EXPERIMENTAL AND ANALYTICAL INVESTIGATION OF THE SIZE
EFFECT ON THE STRENGTH OF OPEN HOLE COMPOSITE LAMINATES

A THESIS SUBMITTED TO
THE GRADUATE SCHOOL OF NATURAL AND APPLIED SCIENCES
OF
MIDDLE EAST TECHNICAL UNIVERSITY

BY

ALI GEZER

IN PARTIAL FULFILLMENT OF THE REQUIREMENTS
FOR
THE DEGREE OF MASTER OF SCIENCE
IN
AEROSPACE ENGINEERING

DECEMBER 2021

Approval of the thesis:

EXPERIMENTAL AND ANALYTICAL INVESTIGATION OF THE SIZE EFFECT ON THE STRENGTH OF OPEN HOLE COMPOSITE LAMINATES

submitted by **ALI GEZER** in partial fulfillment of the requirements for the degree of **Master of Science in Aerospace Engineering Department, Middle East Technical University** by,

Prof. Dr. Halil Kalıpçılar
Dean, Graduate School of **Natural and Applied Sciences** ———————

Prof. Dr. Serkan Özgen
Head of Department, **Aerospace Engineering** ———————

Prof. Dr. Demirkan Çöker
Supervisor, **Aerospace Engineering** ———————

Examining Committee Members:

Prof. Dr. Altan Kayran
Aerospace Engineering, METU ———————

Prof. Dr. Demirkan Çöker
Aerospace Engineering, METU ———————

Prof. Dr. Levend Parnas
Mechanical Engineering, TEDU ———————

Assoc. Prof. Dr. Ercan Gürses
Aerospace Engineering, METU ———————

Assoc. Prof. Dr. Sezer Özerinç
Mechanical Engineering, METU ———————

Date: 10.12.2021

I hereby declare that all information in this document has been obtained and presented in accordance with academic rules and ethical conduct. I also declare that, as required by these rules and conduct, I have fully cited and referenced all material and results that are not original to this work.

Name, Surname: Ali Gezer

Signature   :

ABSTRACT

EXPERIMENTAL AND ANALYTICAL INVESTIGATION OF THE SIZE EFFECT ON THE STRENGTH OF OPEN HOLE COMPOSITE LAMINATES

Gezer, Ali

M.S., Department of Aerospace Engineering

Supervisor: Prof. Dr. Demirkan Çöker

December 2021, 86 pages

In this thesis, we investigate the effect of size on the strength of open hole composite laminates using experimental and analytical approaches. The size effect consists of the effect of thickness and hole size while keeping width to diameter ratio constant.

In the experimental part of this work, tensile tests are conducted on CFRP open hole specimens. In-situ images of the top and side surfaces of the test specimens are captured throughout the experiments and load displacement curves are acquired from the testing machine. The top surface images are captured using high resolution camera and analyzed with digital image correlation (DIC) technique. The side surface images are captured using high speed camera setup and these images and post-mortem microscope images are used to determine failure mechanisms. Finally, in agreement with the literature, size dependence is observed on a plot of failure stress vs. hole size.

On the analytical part of this work, an analytical methodology is developed based on Tan's approach. The stress field is calculated using Lekhnitskii's Formulation and Classical Lamination Theory(CLT). The analytical strength prediction of the open

hole composite laminate is done according to First-Ply-Fiber-Failure(FPFF) methodology. The analytical model performs well compared to other models in the literature in modeling the size dependence of the failure stress on the hole size.

ÖZ

DELİKLİ KOMPOZİT YAPILARDA BOYUTSAL ÖZELLİKLERİN DAYANIM DEĞERLERİNE ETKİSİNİN DENEYSEL VE ANALİTİK OLARAK İNCELENMESİ

Gezer, Ali

Yüksek Lisans, Havacılık ve Uzay Mühendisliği Bölümü

Tez Yöneticisi: Prof. Dr. Demirkan Çöker

Bu çalışmada delikli kompozit yapılarda boyutsal özelliklerin dayanım değerlerine etkisi deneysel ve analitik olarak incelenmiştir. Boyutsal özellikler numune genişliğinin delik çapına oranına sabit tutulduğu numunelerde, kalınlık ve delik çapının etkisini içermektedir.

Deneysel kısımda çekme testleri delikli karbon fiber takviyeli polimer numunelerde icra edilmiştir. Deney numunelerinin üst ve yan yüzey fotoğrafları deney boyunca gerçek zamanlı olarak çekilmiştir ve yük deplasman eğrileri test makinasından elde edilmiştir. Üst yüzey görselleri yüksek çözünürlüklü kamera düzeneği kullanılarak elde edilmiş ve dijital görüntü korelasyon tekniği ile analiz edilmiştir. Yan yüzey görselleri yüksek hızlı kamera düzeneği kullanılarak elde edilmiş ve bu görseller ile deney sonrası elde edilen mikroskobik görseller hasar mekanizmasını belirlemede kullanılmıştır. Literatür ile tutarlı olarak, boyutsal etkiler kırılma anındaki gerilmenin delik çapına karşı olan grafiğinde gözlemlenmiştir.

Analitik kısımda, Tan'ın yaklaşımı kullanılarak bir metot geliştirilmiştir. Stres alanı Lekhnitskii Formülasyonu ve Klasik Laminasyon Teorisi kullanılarak hesaplanmıştır. Analitik delikli kompozit laminat dayanımı ilk tabaka fiber hasarı metodu kullanılarak hesaplanmıştır. Analitik model literatürdeki boyutsal etkilere ve delik çapına bağlı kırılma geriliminin modellendiği diğer modellere göre daha iyi sonuç vermiştir.

Anahtar Kelimeler: dayanım, delikli, kompozit, kırılma, boyutsal etki, analitik modelleme

To my family...

ACKNOWLEDGMENTS

TABLE OF CONTENTS

LIST OF TABLES

TABLES

<div align="center">**LIST OF FIGURES**</div>

FIGURES

xv

xvi

LIST OF ABBREVIATIONS

ASC	Average Stress Criterion
ASTM	American Society for Testing and Materials
CFRP	Carbon Fiber Reinforced Polymer
CLT	Classical Lamination Theory
DIC	Digital Image Correlation
EPSM	Extended Point Stress Method
FPF	First-Ply-Failure
FPS	Frame per Second
FPFF	First-Ply-Fiber-Failure
LEFM	Linear Elastic Fracture Mechanics
OHT	Open Hole Tensile
PSC	Point Stress Criterion
RF	Reserve Factor
RFF	Fiber Reserve Factor
RFM	Matrix Reserve Factor
SCF	Stress Concentration Factor
SR	Strength Reduction
UD	Unidirectional
UNT	Unnotched Tensile

INTRODUCTION

Owing to their high strength-to-weight ratios composite material usage in the design of aircraft structures became more advantageous compared to the metals [1]. In Figure 1.1, the percentage usage of composite materials in commercial airplanes are given [2].
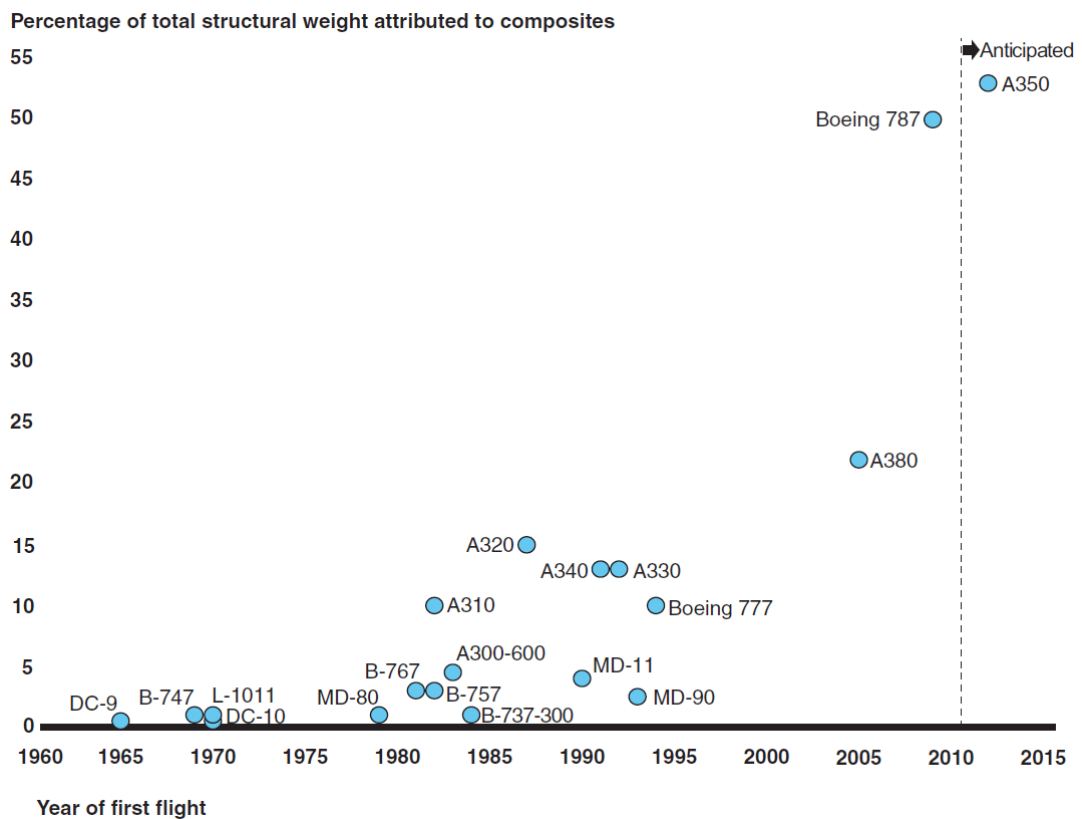
Figure 1.1: Composite usage on commercial airplanes [2].

Throughout the years, composite usage in commercial airplane parts have been in-

creased. Aircraft parts cannot be thought without holes. Holes are needed in aircraft parts for several reasons: to bolt removable parts, to allow system installation parts to pass through them, such as wires and tubes. By virtue of these reasons, stress concentrations are needed to be involved into the design phases. In Figure 1.2, some example composite aircraft parts are shown [3][4]. The main barrier on the widespread us-

Figure 1.2: Example composite parts of (top) A350 and (bottom) XB-1 [3][4].

age of composites on the aircraft structures is strength certification. The certification procedure is expensive and challenging period on the design phase of the aircraft. As shown in Figure 1.3, certification process starts with coupon tests [5].
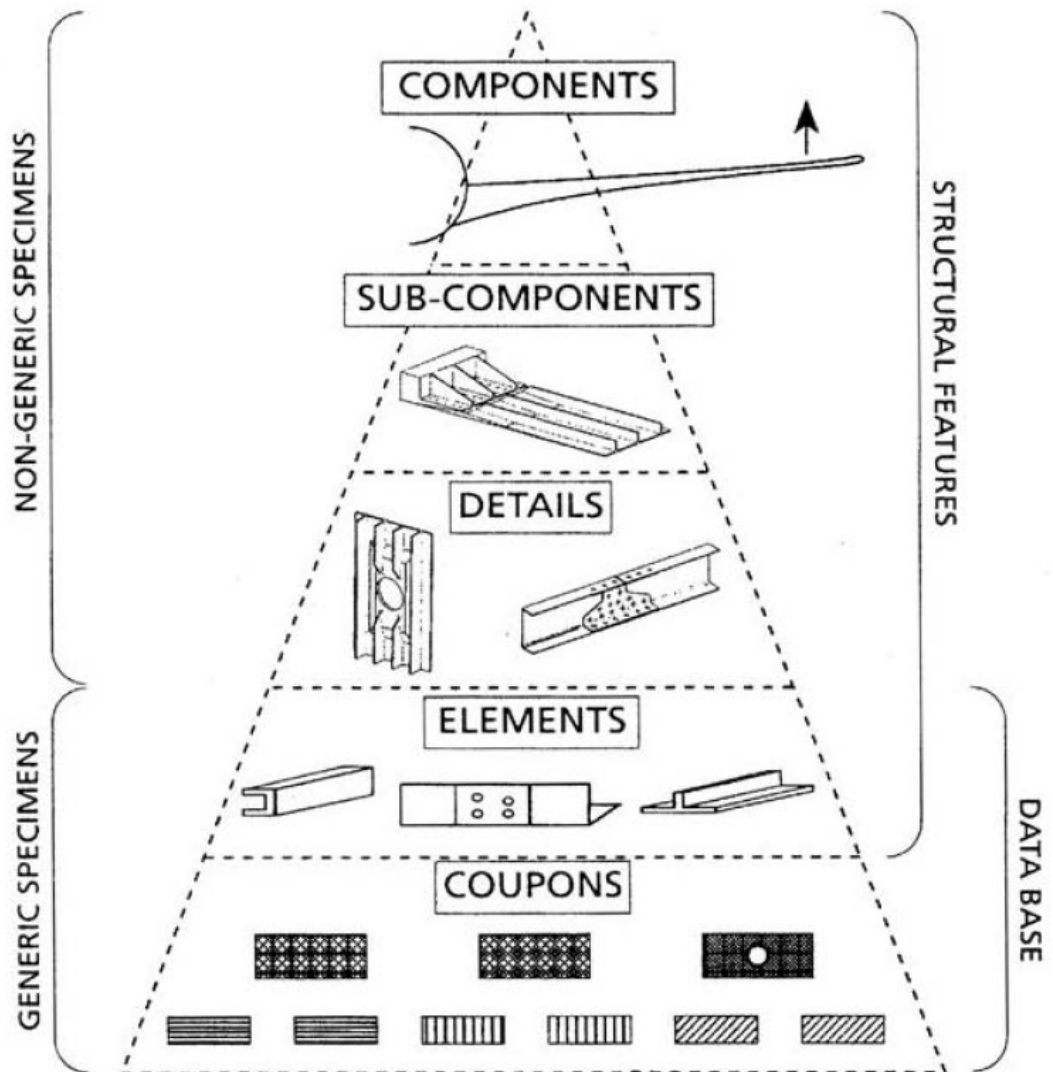
Figure 1.3: Schematic diagram of certification tests [5].

The coupon tests are used to certify design methodologies. The design methodologies can involve simple or detailed models. The simple models can be used with limited accuracy and applicability. On the other hand, the detailed models are more accurate. However, the detailed models are more time consuming and expensive.

The aim of the study contained herein is to investigate the size effects on the strength of open hole composite laminates experimentally and analytically. Set of experiments are conducted to examine the size effect of hole size and laminate thickness on the notched strength of open hole composite laminates. The information gathered from the series of tests is used to understand damage that occurs within the laminates. The results of the experiments are compared to well-known analytical methods and proposed analytical methodology. Novelties of the experimental findings and the proposed analytical methodology are given.

CHAPTER 2

THEORETICAL BACKGROUND

There are various studies in literature for obtaining stress states in composite laminates containing holes. Several comprehensive review papers of the existing methodologies can be found in literature such as the ones by Awerbuch and Nahas [6][7]. These studies followed two main paths; analytical and numerical approaches. The numerical methodologies have proceeded to the point where the failure criteria have been fully established. However, these failure criteria are used very rarely in the engineering applications. The reason of that resides in the impractical determination of the material failure properties, required in applying these failure criteria, and lack of analytical expressions of either stress or strain state of the composite laminates containing holes. By perceiving these limitations, researchers are dug into the topic of notched strength prediction of the composite laminates containing holes or notches. The aim is to come up with strength prediction models or criteria in order to determine the failure of commonly used structural components.

In this chapter, well known analytical approaches and previous experiments are examined. The analytical approaches and the previous experimental studies are taken as the basis for the establishment of the proposed methodology and experimental procedure of this study which explained in details in Chapter 3 and 4.

2.1 Analytical Approaches

Analytical attempts start with Waddoups et al. [8], who utilized linear elastic fracture mechanics(LEFM) for the open hole strength prediction of composite laminates. LEFM is based on the assumption that, damage mechanisms occurring just before ultimate failure can be lumped into a "region of intense energy" called "inherent flaw" of length a as depicted in Figure 2.1. After this assumption, the critical value of the stress intensity factor of an open hole laminate is

$$K_{IC} = f(a, R)\overline{\sigma}\sqrt{\pi a} \tag{2.1}$$

where $f(a, R)$ is Bowie's solution for the two cracks originating from the circular hole[9]. R and $\bar{\sigma}$ denote hole radius and remote applied stress, respectively. For the unnotched specimen, $f(a, R)$ can be taken as 1. In this case, K_{IC} is

$$K_{IC} = X_L{}^T\sqrt{\pi a} \tag{2.2}$$

where $X_L{}^T$ is the tensile strength of the laminate. After equating Eqs. (2.1) and (2.2), the remote stress $\bar{\sigma}$ is

$$\overline{\sigma} = \frac{X_L{}^T}{f(a, R)} \tag{2.3}$$

Provided that the hole diameter of the laminate is known, Eq. (2.3) shows that the remote stress $\bar{\sigma}$ depends on the characteristic length of the intense energy region, a, and the laminate unnotched strength, $X_L{}^T$.

After Waddoups et al., Whitney and Nuismer [10] introduced two stress criteria, namely point stress criterion(PSC) and average stress criterion(ASC), for the evaluation of stresses in laminated composites containing open holes. Using the stress criteria, size effects of the discontinuities on the strength of the lamina are calculated without referring to LEFM. In their approaches, they used the stress distribution around the hole concept proposed by Timoshenko and Goodier as a basis [11]. The change of normal stress σ_y, along the x axis, with respect to the uniform tensile stress $\bar{\sigma}$, is applied parallel to the y axis at infinity, of an isotropic plate with an open hole is given by

$$\frac{\sigma_y}{\overline{\sigma}} = 1 + \frac{1}{2}\left(\frac{R}{x}\right)^2 + \frac{3}{2}\left(\frac{R}{x}\right)^4$$
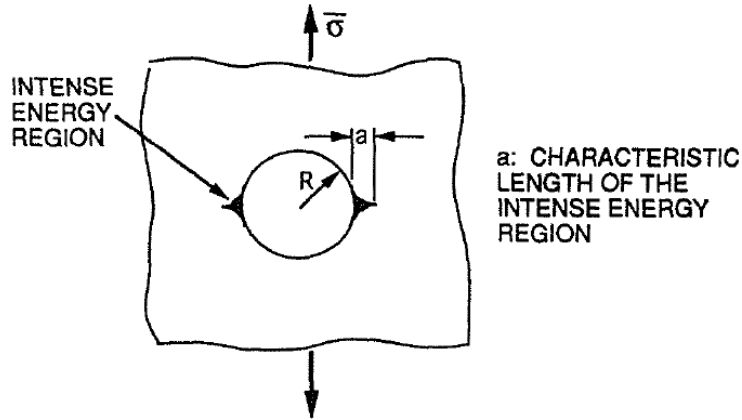
Figure 2.1: Waddoups-Eisenmann-Kaminski Criterion [8].

where R is the radius of the hole and x is the distance in front of the hole. In Figure 2.2, variation of the normalized stress $\frac{\sigma_y}{\bar{\sigma}}$ versus the distance ahead of the hole $(x - R)$ in an infinite isotropic plate is shown.
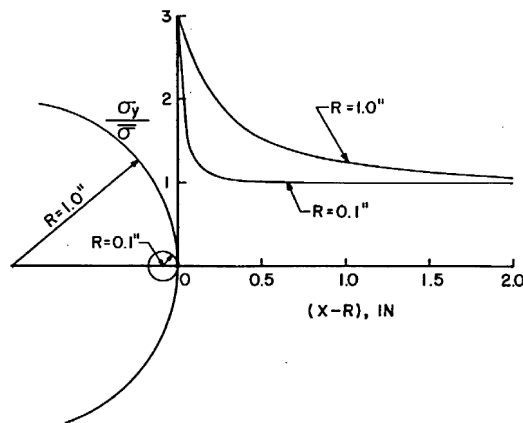
Figure 2.2: Variation of the normalized stress $\frac{\sigma_y}{\bar{\sigma}}$ versus the distance ahead of the hole $(x - R)$ in an infinite isotropic plate [10].

It observed from Figure 2.2 that stress concentration factors(SCFs) is the same for the small and large hole sizes. Yet the stress varies sharply in the vicinity of the smaller hole compared to the larger hole. Therefore, determination of the strength of a brittle material from the maximum stress value is questionable. From this point of view Whitney and Nuismer come up with two approaches for the prediction of the strength of laminated composites with discontinuities. These criteria illustrated in Figure 2.3.

7
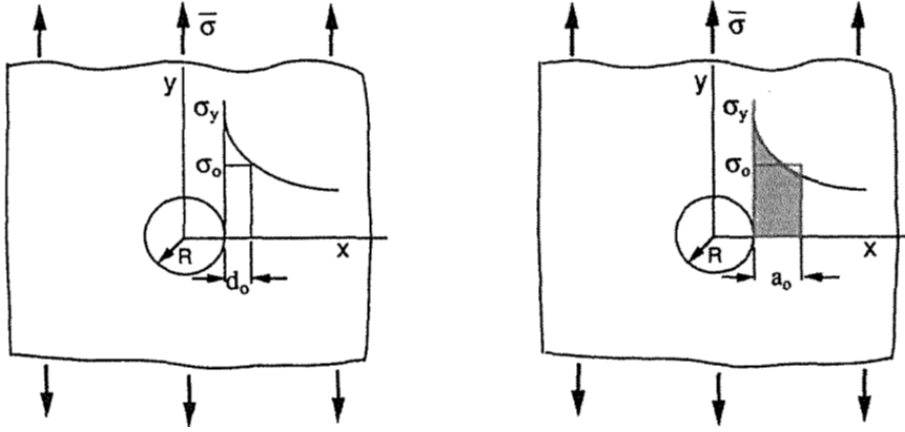
Figure 2.3: Illustration of PSC and ASC [12].

In the PSC, failure occurs when the point stress value is equal to or greater than the strength of the unnotched laminate at some distance d_0 away from the discontinuity. Strength ratio using PSC for the case of a circular hole in an isotropic plate is

$$\frac{\sigma_N}{\sigma_0} = \frac{2}{2 + \xi_1^2 + 3\xi_1^4} \quad , \quad \xi_1 = \frac{R}{R + d_0}$$

where σ_N is the laminate notched strength, σ_0 is the laminate unnotched strength.

In the ASC, failure occurs when the average stress value is equal to or greater than the strength of the unnotched laminate at some distance a_0 away from the discontinuity. Strength ratio using ASC for the case of a circular hole in an isotropic plate is

$$\frac{\sigma_N}{\sigma_0} = \frac{2(1 - \xi_2)}{2 - \xi_2^2 - \xi_2^4}$$

where

$$\sigma_0 = \frac{1}{a_0} \int_R^{R+a_0} \sigma_y(x, 0)dx \quad , \quad \xi_2 = \frac{R}{R + a_0}$$

Above mentioned distances, d_0 and a_0, are called as characteristic distances and considered as material property independent of laminate geometry and stress distribution. R is the hole radius.

Based on the point stress failure model, Karlak proposed a modified method [13]. Based on his experimental observations, he concluded that the characteristic distance

8

is also related to the square-root of the hole rather than the material. In this regard, characteristic distance relation is proposed by Karlak as shown below.

$$d_0 = k_0 \sqrt{R}$$

where R is the hole radius and k_0 is the parameter which depends on the laminate configuration and material properties. This parameter must be experimentally determined.

Pipes et al. extended the relation developed by Karlak and included notch sensitivity parameter in their formulation [14]. In this three parameter relation,

$$d_0 = C R^m$$

C is the material and lay-up dependent constant, R is the hole radius and m is the notch sensitivity parameter. Values of C and m need to be determined by experiments. If the value of m equals to zero ($m = 0$), characteristic distance is a constant value and relation recovered to Whitney-Nuismer PSC. And in case that value of m equals to one ($m = 1$), characteristic distance is not affected by the notch size. In other words, notch sensitivity is not considered.

After the first stress models, which are limited to infinite isotropic plates, Konish and Whitney came up with an approximate solution in the form of polynomial for the stress distribution for an infinite orthotropic plate containing hole [15].

$$\sigma_y(x,0) = \frac{\overline{\sigma}}{2} \left\{ 2 + \left(\frac{R}{x}\right)^2 + 3\left(\frac{R}{x}\right)^4 - (K_T^\infty - 3)\left[5\left(\frac{R}{x}\right)^6 - 7\left(\frac{R}{x}\right)^8\right] \right\}$$

where

$$K_T^\infty = 1 + \sqrt{\frac{2}{A_{22}}\left[\sqrt{A_{11}A_{22}} - A_{12} + \frac{A_{11}A_{22} - A_{12}^2}{2A_{66}}\right]}$$

where K_T^∞ stands for the orthotropic stress concentration factor for an infinite width plate. $A_{ij}(i,j = 1,2,6)$ are the components of extensional stiffness matrix. K_T^∞ can also be written as in terms of engineering constants [12].

$$K_T^\infty = 1 + \sqrt{2\left(\sqrt{\frac{E_2}{E_1}} - \nu_{21}\right) + \frac{E_2}{G_{12}}}$$

where E_1, E_2, G_{12} and ν_{21} are effective orthotropic elastic constants of the laminate.

Tan take into account the work done by Konish and Whitney and introduce the approximate orthotropic finite width correction factor [12].

$$\frac{K_T^\infty}{K_T} = \frac{3\left(1 - D/W\right)}{2 + \left(1 - D/W\right)^3} + \frac{1}{2}\left(\frac{D}{W}M\right)^6 \left(K_T^\infty - 3\right)\left[1 - \left(\frac{D}{W}M\right)^2\right]$$

where

$$M = \sqrt{\frac{\sqrt{1 - 8\left[\frac{3(1-D/W)}{2+(1-D/W)^3} - 1\right]} - 1}{2\left(D/W\right)^2}} \quad , \quad D = 2R$$

By taking into account stress distribution and finite width stress concentration factor for orthotropic finite plate containing hole, PSC and ASC can be written as

$$\frac{\sigma_N}{\sigma_0} = \frac{2}{2 + \xi_1^2 + 3\xi_1^4 - \left(K_T - 3\right)\left(5\xi_1^6 - 7\xi_1^8\right)} \quad , \quad PSC \tag{2.4}$$

$$\frac{\sigma_N}{\sigma_0} = \frac{2\left(1 - \xi_2\right)}{2 - \xi_2^2 - 3\xi_2^4 + \left(K_T - 3\right)\left(\xi_2^6 - \xi_2^8\right)} \quad , \quad ASC \tag{2.5}$$

Tan extended the application zone of stress-failure models and developed a new model for the strength prediction of composite laminates containing an opening under combined in-plane loading [16]. He predicted the strength reduction using the first-ply-failure(FPF) stress. Strength reduction model for the notched laminate under combined in-plane loading calculated as

$$SR = \frac{\sigma_N}{\sigma_0} = \frac{FPF\left(Notched\right)\left|at\frac{x^2}{(a+b_0)^2} + \frac{y^2}{(b+b_0)^2} = 1\right.}{FPF\left(Unnotched\right)}$$

Tan dictated that, this model is not appropriate if the failure modes of the laminates with different hole sizes are not the same. For matrix-dominated laminates FPF can be used for the notched strength prediction. For fiber-dominated laminates first-ply-fiber-failure(FPFF) can be used for the notched strength prediction.

$$SR = \frac{\sigma_N}{\sigma_0} = \frac{FPFF\left(Notched\right)\left|at\frac{x^2}{(a+b_0)^2} + \frac{y^2}{(b+b_0)^2} = 1\right.}{FPFF\left(Unnotched\right)}$$

Tan used Tsai-Wu quadratic failure criterion for the FPF analysis while below criterion applied for the FPFF analysis [17].

$$\frac{\sigma_1^2}{X_T X_C} + \sigma_1\left(\frac{1}{X_T} - \frac{1}{X_C}\right) = e^f \tag{2.6}$$

10

where σ_1 denotes the lamina normal stress in the fibers direction. X_T and X_C denote longitudinal tensile and compressive strength, respectively. If any ply within a laminate satisfies the condition: $e_f \geqq 1$, the ultimate failure is considered occurred.

Tan's approach requires the lamina stresses for the strength prediction of the notched laminate. Lamina stresses can be found from the Classical Lamination Theory(CLT). In order to find laminate stresses, Lekhnitskii complex variable mapping method can be used. Details of CLT and Lekhnitskii complex variable mapping method are given in the appendices chapter.

2.2 Experiments on Size and Notch Effect

Many experiments are conducted in the field of open hole composite laminates to understand effect of size and hole effects on the notched strength. Various authors [6][8][10][18][19] investigated the notch size effect on the strength for a constant specimen width. The decrease in strength with increasing notch size is observed for constant width specimens. Awerbuch and Madhukar observed that, notch sensitivity is affected by different variables. Such as laminate configuration, stacking sequence, specimen geometry, etc. Moreover, they also focused on sub-critical, prior to failure, damage phenomena at the notch and its effect on the notch sensitivity in their following works.

Lagace investigated notched strength dependency on stacking sequence [20]. In the light of conducted experiments on graphite/epoxy specimens, he suggested that variations in notched strength on different stacking sequences could be result of changes in the interlaminar stresses present in a laminate, which leads to change of failure mechanism from a fibre dominant to matrix dominant. In the experiments, three different stacking sequences $[\pm\theta/0]_s$, $[0/\pm\theta]_s$ and $[+\theta/0/-\theta]_s$ for θ values between $15°$ and $90°$ with four different circular hole sizes $3.175mm$, $6.35mm$, $9.525mm$ and $12.7mm$ are investigated. For $\theta < 45°$, little or no delamination was observed. However, failure stresses are varied between the different stacking sequences. For $\theta = 45°$, no significant differences between different stacking are observed. For $\theta > 45°$, delamination prior to failure is observed on $[0/\pm\theta]_s$ and $[+\theta/0/-\theta]_s$

stacking sequences. $[+\theta/0/-\theta]_s$ stacking sequence shown no delamination and has highest notched strength compared to other two stacking sequences. It can be deduced that, stacking sequence has an influence on the notched strength and the failure mechanism of composite laminates.

Harris and Morris [21][22] studied the influence of laminate thickness on the notched strength of composite laminates. In their research, thickness of the laminate is increased by stacking the sublaminate blocks. Ply thicknesses are kept constant. Consequently, strength reduction with increasing the laminate thickness is observed for $[0/\pm45/90]_{ns}$ stacking sequences. Contrary to this observation, strength increase with increasing the laminate thickness is observed for $[0/\pm45]_{ns}$. For $[0/\pm45/90]_{ns}$ laminates, the notched strength is reduced with increasing the laminate thickness due to change in crack-tip damage. Experimental observations shown that at the same load levels, size of the crack-tip damage is decreasing with increasing the laminate thickness. Therefore, as the laminate gets thicker, stress redistribution is reduced and notched strength is lessened. For $[0/\pm45]_{ns}$ laminates, the notched strength is increased with increasing the laminate thickness. Delamination driven failure mechanism is prevented as the thickness of the laminate increased. Therefore, as the laminate gets thicker, failure mechanism is changed from matrix dominant to fiber dominant.

An extensive research campaign on investigation into the scaling size effect of notched composites conducted by Green et al. [23]. Two different scaling methodology on thickness of the laminate are examined namely, sublaminate-level and ply-level scaling. In sublaminate-level scaling, the laminate thickness is increased by repeating the initial stacking sequence. In ply-level scaling, the laminate thickness is increased by increasing the number of same oriented plies. In Figure 2.4, the scaling methodology and testing matrix are shown.

	Sublaminate-level Scaling				Ply-level Scaling			
	Hole diameter (mm)				Hole diameter (mm)			
t (mm)	3.175	6.35	12.7	25.4	3.175	6.35	12.7	25.4
1								
2	1D	3D						
4		2D						
8								

Figure 2.4: Sublaminate and ply-level scaling methodology [23].

Ply-level scaled specimens showed either a pull-out or, in most cases, delamination type failure. Sublaminate-level scaled specimens have failed by fiber failure for all specimen sizes, with either a pull-out or brittle appearance. Failure mechanism are shown in Figure 2.5.

Brittle   Pull-out   Delamination
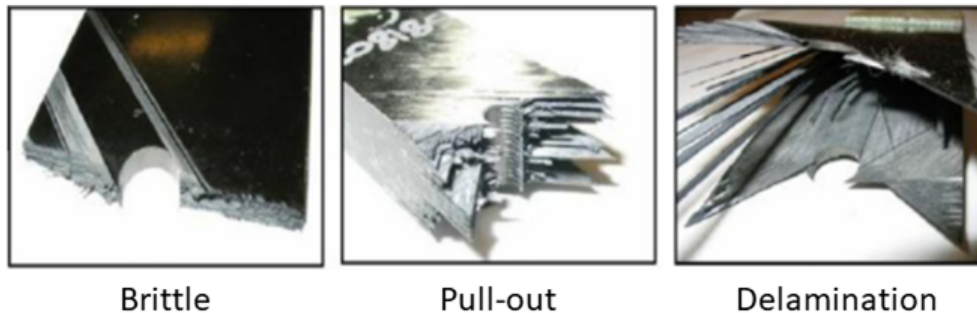
Figure 2.5: Failure mechanism of sublaminate and ply-level scaled laminates [23].

Green et al. [23] also made observations on sub-critical damage development in open hole CFRP laminates. In their work, the sub-critical damage splitted into four separate stages in that sequence: isolated matrix cracks at the hole, damage accumulation at the hole(inner delamination regions), damage growth through the width of the specimen(outer delamination regions) and final damage along the length of the specimen. These damage zone stages can be seen in Figure 2.6.
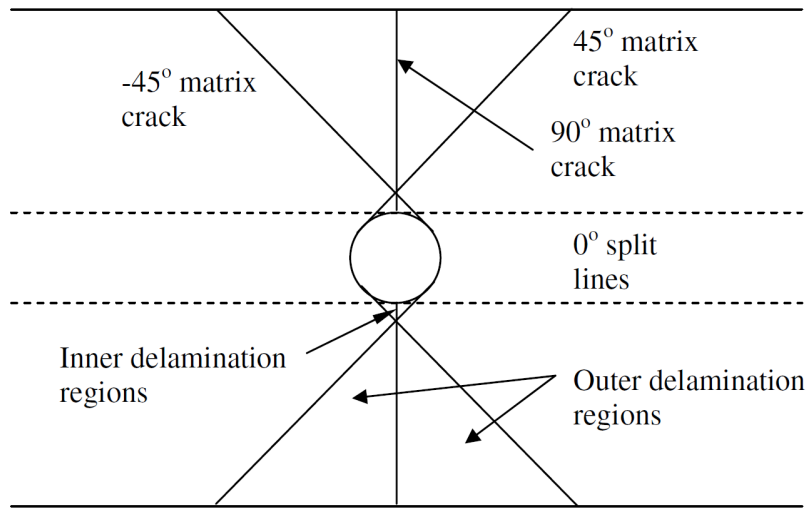
Figure 2.6: The sub-critical damage zones [23].

Firstly, matrix cracks in the $90°$ plies are observed at the hole boundary. Then, isolated matrix cracks occurring in off-axis plies. The matrix cracks are followed by splitting in the $0°$ plies. In the adjacent interfaces, local delaminations occurred. In the next stage, the isolated cracks, splits and delaminations join together. Those delaminations allow the crack propagation through the width. In the sublaminate-level scaled specimens, crack propagation through the width was restrained by the $0°$ plies. After the damage propagation across the width of the specimen, isolated matrix cracks and delaminations appeared first. That damage is remained within the outer delamination regions. At the end, matrix cracks, splits and delaminations were seen at the edge of the specimen away from the outer delamination regions.

In the experiments, sub-critical damage mechanisms are observed on all specimen sizes regardless the scaling method. In the sublaminate-level scaled specimens, as the hole size is increased, very little sub-critical damage is occurred. Therefore, stress redistribution is reduced and the specimen is failed at a lower stress.

CHAPTER 3

ANALYTICAL METHOD

For the analytical strength analysis of the open hole composite laminates, an analytical methodology is developed based on the Tan's approach which is an extended version of Whitney-Nuismer Stress-Failure Model [12]. Hereafter, the proposed methodology called as Extended Point Stress Method(EPSM). Tan introduces an analytical model for the strength prediction of notched laminated composites subjected to in-plane combined loading, which is depicted in Figure 3.1. Characteristic curve, b_0, is represented by a dashed elliptical curve. $\overline{\sigma}_x$, $\overline{\sigma}_y$ and $\overline{\tau}_{xy}$ are the average plane stress values with respect to laminate thickness.

$$\overline{\sigma}_x = \frac{1}{h} \int_{-h/2}^{h/2} \sigma_x dz \qquad \overline{\sigma}_y = \frac{1}{h} \int_{-h/2}^{h/2} \sigma_y dz \qquad \overline{\tau}_{xy} = \frac{1}{h} \int_{-h/2}^{h/2} \tau_{xy} dz$$

Figure 3.1: Notched laminated composite model subjected to multiaxial loading [17].

15

Strength reduction(SR) of the model is calculated using

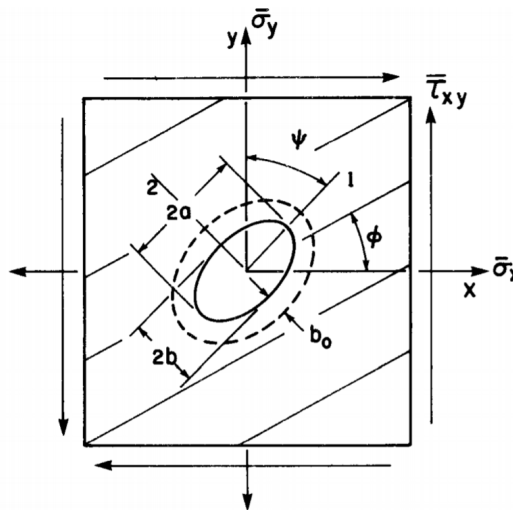$$SR = \frac{\sigma_N}{\sigma_0} = \frac{FPFF\,(Notched)\,\left|at\,\frac{x^2}{(a+b_0)^2} + \frac{y^2}{(b+b_0)^2} = 1\right.}{FPFF\,(Unnotched)} \tag{3.1}$$

In Eq. (3.1), σ_N and σ_0 are the notched ultimate strength and unnotched laminate strength, respectively. The characteristic curve, b_0 needs to be determined experimentally. The notched ultimate strength of the laminate is calculated by multiplying SR with unnotched laminate strength.

In this study, combination of Yamada-Sun and Puck iterative failure criterion is implemented for calculating reserve factor(RF) of the unnotched laminate, whereas Tsai-Wu quadratic failure criterion is used for calculating strength ratio(SR) of the notched laminate. Algorithm of the proposed methodology is depicted in Figure 3.2.

Material properties, laminate geometry and load cases are given as input. For the unnotched laminate, layer stresses are found using the classical lamination theory(CLT), whereas for the notched laminate, firstly stress field is generated using Lekhnitskii complex variable mapping method. Then, the layer stresses are obtained at characteristic distance, d_0, using CLT. Details of the Lekhnitskii complex variable mapping method and CLT are given in Appendix A and Appendix B. For this study, the point stress criterion(PSC), refer to Eq. (2.4), is chosen to find the characteristic distance where unnotched and notched strength of the laminate are the required inputs.

Then, the characteristic distance is modified as

$$d_0 = d_{0_{ref}} \left(\frac{D}{D_{ref}}\right)^n \tag{3.2}$$

where $d_{0_{ref}}$ is the reference characteristic distance found by using PSC, D and D_{ref} are tested specimen hole diameter and reference specimen hole diameter, respectively. n is the notch sensitivity factor.

Once the layer stresses are obtained for the unnotched and the notched laminate, the reserve factors can be calculated for the given load case. As it shown in Figure 3.2, the reserve factors are found based on two failure criteria. As suggested in Tan's work, the Tsai-Wu quadratic failure criterion, Eq. (2.6) is used for the first-ply-fiber-failure(FPFF) analysis.
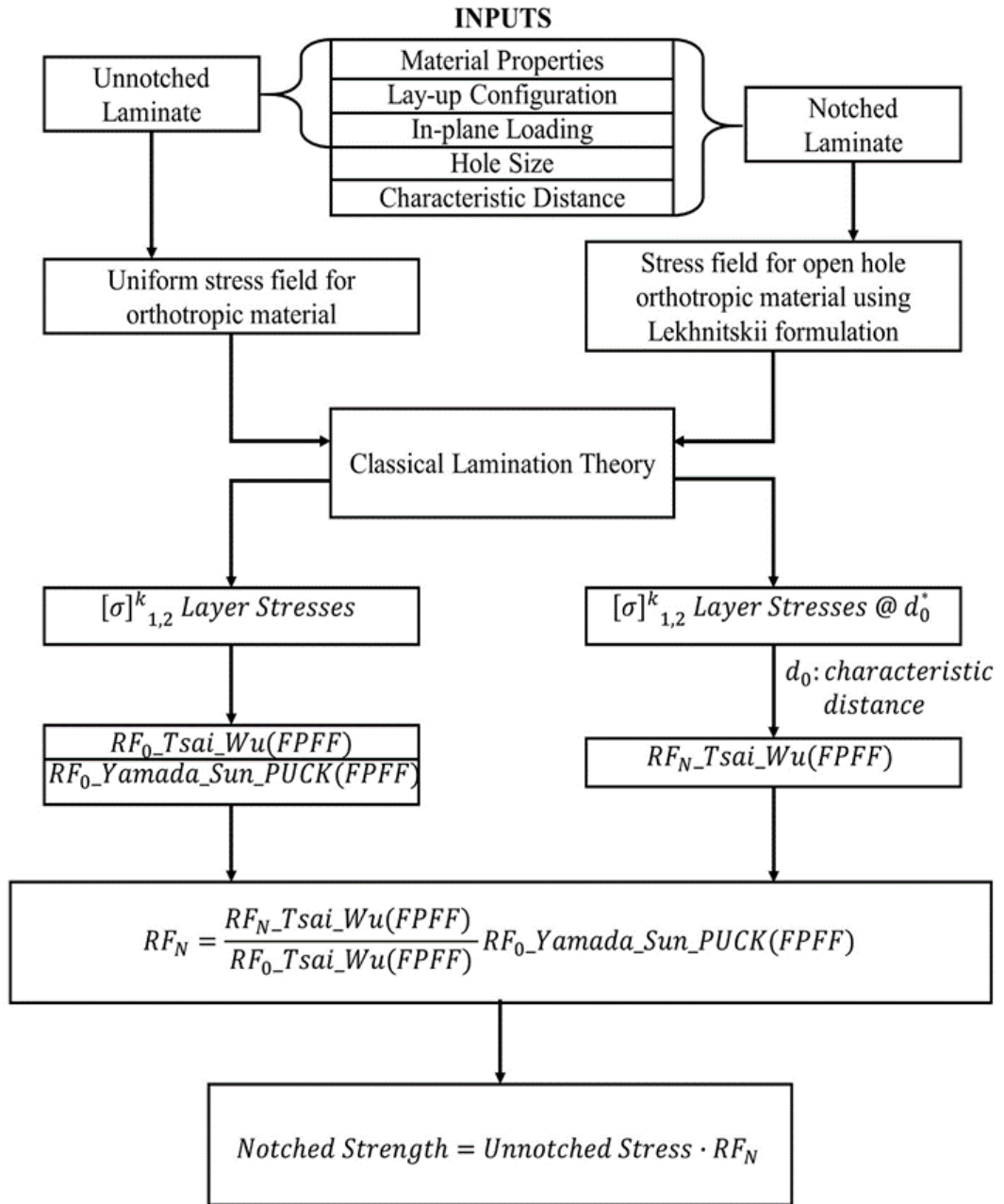
Figure 3.2: Analytic flowchart for the prediction of composite laminate notched strength.

The reserve factor of the unnotched laminate is found combining the Yamada-Sun and Puck failure criteria. The Yamada-Sun and Puck composite failure criterion is an iterative approach and based on the reduction of the laminate stiffness due to matrix-failure and fiber-failure. The Yamada-Sun failure criterion is used for the fiber-failure [24]

$$\left(\frac{\sigma_1}{X}\right)^2 + \left(\frac{\tau_{12}}{S}\right)^2 = l^2, \quad l \geq 1 \quad failure$$
$$X = X_T \quad if \quad \sigma_1 \geq 0 \quad , \quad X = X_C \quad if \quad \sigma_1 < 0$$
(3.3)

where σ_1 and τ_{12} are longitudinal and shear stresses, respectively. X is the lamina, tensile or compressive strength in longitudinal direction and S is shear strength of the lamina.

Modified puck criterion is used for the matrix-failure [25][26]

$$\underbrace{\left(\frac{\sigma_1}{2X_T}\right)^2}_{*} + \frac{\sigma_2^2}{Y_T Y_C} + \left(\frac{\tau_{12}}{S}\right)^2 + \left(\frac{1}{Y_T} + \frac{1}{Y_C}\right)\sigma_2 = 1$$
(3.4)

where σ_1, σ_2 and τ_{12} are longitudinal, transverse and shear stresses respectively. X_T represents longitudinal tensile strength and S is shear strength. Y_T and Y_C denote transverse tensile and compressive strength, respectively. The term $(*)$ is not always included in the modified Puck criterion found in literature. This term helps to include the parallel-to-fiber stress, σ_1, in the matrix failures. Sometimes micro fiber fractures cause local debonding between the fiber and the matrix, which in turn reduce the fiber matrix cohesion. As a consequence, matrix resistance to failures reduces [27].

Using Eqs. (2.6), (3.3) and (3.4), reserve factors of each lamina are found as follows. For the Tsai-Wu criterion, the reserve factor of the lamina can be found from

$$RF^2\left(\frac{\sigma_1^2}{X_T X_C}\right) + RF\left(\frac{1}{X_T} - \frac{1}{X_C}\right)\sigma_1 = 1$$
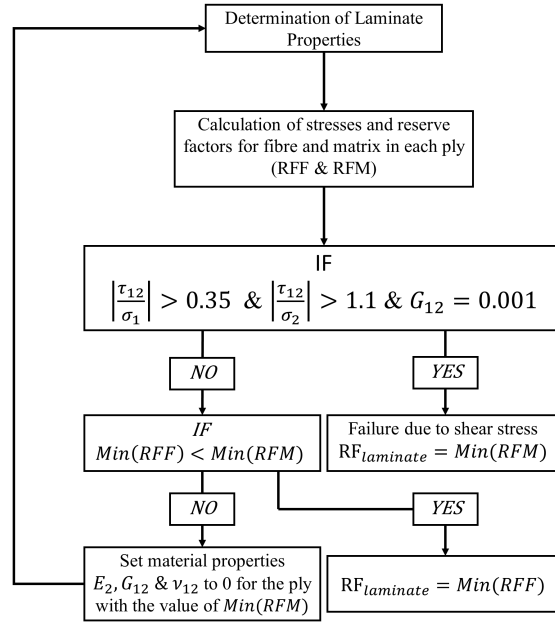
Figure 3.3: Flowchart for the progressive failure analysis of composite unnotched strength.

For the composite failure criterion the matrix and the fiber reserve factors of each lamina should be obtained. Progressive failure analysis based on the composite failure criterion is represented in Figure 3.3.

The fiber reserve factor(RFF) of the lamina can be found from

$$\left(\frac{\sigma_1 RFF}{X}\right)^2 + \left(\frac{\tau_{12} RFF}{S}\right)^2 = 1$$

$$X = X_T \;\; if \;\; \sigma_1 \geq 0 \;\;, \;\; X = X_C \;\; if \;\; \sigma_1 < 0$$

The matrix reserve factor(RFM) of the lamina can be found from

$$RFM^2 \left[\left(\frac{\sigma_1}{2X_T}\right)^2 + \frac{\sigma_2^2}{Y_T Y_C} + \left(\frac{\tau_{12}}{S}\right)^2 \right]$$

$$+ RFM \left(\frac{1}{Y_T} + \frac{1}{Y_C}\right) \sigma_2 = 1$$

By following progressive analysis algorithm, which depicted in Figure 3.3, reserve factor of the laminate can be found.

19

Using the unnotched and the notched reserve factors of the laminate, RF_N is obtained. The unnotched stress is defined as

$$Unnotched\ Stress = \frac{Applied\ Load}{Laminate\ Thickness}$$

The notched strength is found by multiplying the RF_N and the unnotched stress.

CHAPTER 4

EXPERIMENTAL METHOD

An extensive test campaign is conducted to accomplish the main indent of this research. With the help of experimental results the developed method and extend of the size effect on the laminates containing hole are evaluated. Open hole test specimens are tested under quasi-static condition. During the experiments, in-situ data are acquired directly from the testing machine and the high speed and high resolution camera systems. The testing machine is recorded the load-displacement data throughout the experiments. The two different camera are focused on the top and the side surface of the test specimens. The top surface images are used on digital image correlation(DIC) technique. The side surface images are used to determine failure mechanism. Details of the experimental method is given in the following sections.

4.1 Material

The material chosen for this research is M91/IM7/34RC/UD/194/12K, an unidirectional(UD) tape carbon fibre reinforced epoxy prepreg, supplied by Hexcel. This material was chosen due to its practical use in aerospace industry. The nominal ply thickness is $0.184mm$ and most of the required properties of this material taken from supplier provided data sheet [28] and research done by Bogenfeld et al. [29] and are given in Table 4.1.

Table 4.1: Mechanical Properties of M91/IM7/34RC/UD/194/12K.

Property		Mean Value
Longitudinal Modulus(MPa)	E_1	170000
Transverse Modulus(MPa)	E_2	8800
In-plane Shear Modulus(MPa)	G_{12}	5500
Poisson's Ratio	ν_{12}	0.228
Longitudinal Tensile Strength(MPa)	X_T	2700
Longitudinal Compressive Strength(MPa)	X_C	1590
Transverse Tensile Strength(MPa)	Y_T	105
Transverse Compressive Strength(MPa)	Y_C	252
In-plane Shear Strength(MPa)	S	105

4.2 Specimen Design

4.2.1 Specimen Geometry

The unnotched and open hole test specimens are designed according to ASTM D3039 [30] and ASTM D5766 [31] standards. The design of the specimens are depicted in Figure 4.1.
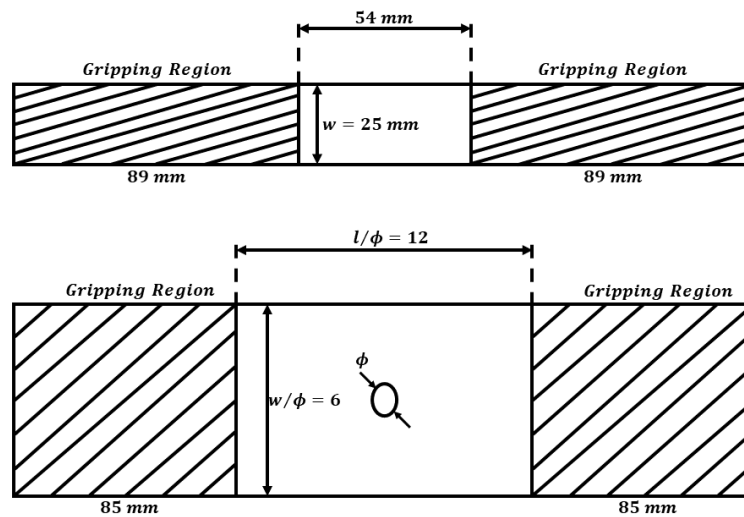
Figure 4.1: Test specimen dimensions.

The unnotched test specimens have constant width and length of $25\ mm$ and $232\ mm$, respectively. At the gripping regions, tabs are used. The open hole test specimens have constant ratios of $w/\phi = 6$ and $l/\phi = 12$ at the gage section for all specimens. Since the holes are natural stress risers, end tabs are not used. Above mentioned geometrical values are selected to fulfill minimum required distances to allow the stress levels close to uniform values at the edges. By doing that, material usage is minimized.

4.2.2 Stacking Sequence

The stacking sequence for this study is selected as $[+45/0/-45/90]_s$. This lay-up is generally preferred in aircraft design. Main reason is that to protect main load-carrying plies from impact damage. Also, previous experiences show that this lay-up mostly failed due to the fiber failure. This failure mechanism made this lay-up perfect candidate to validate the proposed analytical methodology.

4.2.3 Sizing Methodology

In this study effect of two different sizes are examined. These are thickness and in-plane sizing. In literature [23] two different methods exist to increase the thickness of the specimens. These are sublaminate and ply-level scaling. In the sublaminate-level scaling, the thickness of the specimen increased by repeating the master stacking sequence. The sublaminate-level scaled specimens can be designated as $[+45/0/-45/90]_{ns}$. In the ply-level scaling, the thickness of the specimen increased by blocking the same oriented plies. The ply-level scaled specimens can be designated as $[+45_m/0_m/-45_m/90_m]_s$. Above mentioned scaling methodologies are illustrated in Figure 4.2.
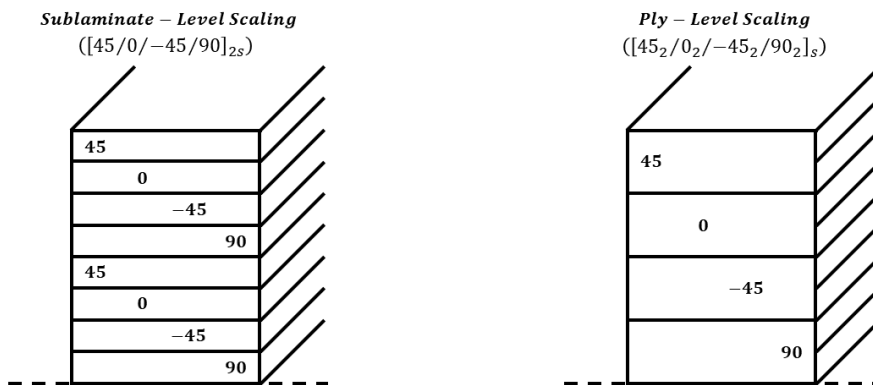

Figure 4.2: Sublaminate and ply-level scaling techniques.

In literature [23], it observed that the ply-level scaling led to delamination failure most of the cases. On the other hand, the sublaminate-level scaling specimens shown pull-out and brittle failure. To support validation studies of the analytical methodology, the sublaminate-level scaling technique is used to observe the thickness size effect.

In-plane sizing is done by using various hole sizes. The minimum and the maximum hole sizes are selected as $3.175mm$ and $25.4mm$, respectively. These hole sizes are the most known and used ones in the aerospace industry. The width and the length of the specimens are varied with the change of the hole size while kept the constant w/ϕ and l/ϕ ratios at the gage sections. In Table 4.2, the gage section properties of the specimens are given.

Table 4.2: Gage section properties of the specimens for the different hole sizes.

Hole Size, ϕ (mm)	Width, w (mm)	Gage Length, l (mm)
3.175	19.05	38
4.83	28.98	58
6.35	38.1	76
12.7	76.2	152

In order to see the thickness and the in-plane sizing effects, with least amount of testing specimens, testing matrix is generated as shown in Table 4.3.

Table 4.3: Testing matrix of the open hole tensile test specimens.

t (mm)	Specimen Set	Stacking Sequence	Hole Size, ϕ (mm)				
			3.18	4.83	6.35	12.7	25.4
1.472	OHT1	$[+45/0/-45/90]_s$	■				
2.944	OHT2	$[+45/0/-45/90]_{2s}$	■	■	■	■	■
4.416	OHT3	$[+45/0/-45/90]_{3s}$	■	■	■	■	
5.888	OHT4	$[+45/0/-45/90]_{4s}$	■		■	■	

In Table 4.3, across the rows, the hole size and across the columns, the specimen thickness is vary. The thickness and the hole size of base specimen selected as $1.472mm$ and $3.18mm$, respectively. Other specimens are scaled according to these base values. In Figure 4.3, designation rules of the specimens are depicted.

$$OHT1 - 1 - 1$$

Thickness Scaling
1: 1.472 mm
2: 2.944 mm
3: 4.416 mm
4: 5.888 mm

Specimen No
Hole Scaling
1: 3.18 mm
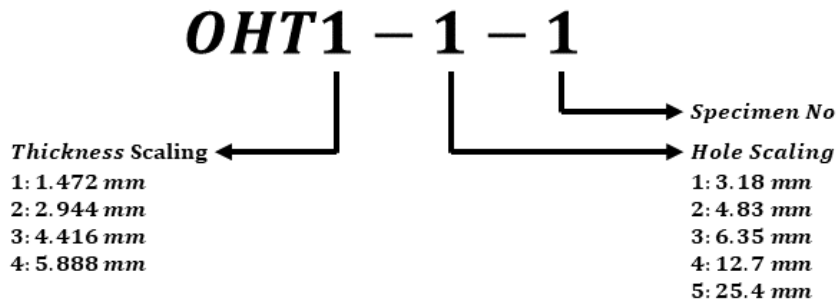2: 4.83 mm
3: 6.35 mm
4: 12.7 mm
5: 25.4 mm

Figure 4.3: Designation of test specimens.

First dash number indicates the thickness, second dash number indicates the hole size and third dash number indicates the specimen number on batch.

4.3 Manufacturing Process

The test specimens are manufactured by using hand lay-up technique. Lay-up procedure starts with preparation of lay-up mandrel surface. Before and after each manufacturing process the lay-up mandrel surface shall be cleaned. After that parting lacquers and parting agents are applied to facilitate removal of parts from the lay-up mandrels. Dry peel ply applied between the lay-up mandrel and first ply. Other plies are applied according to the lay-up sequence configurations. Again as a final layer the dry peel ply is applied. During the laying-up procedure, compaction performed for the first ply down and every fifth ply thereafter to achieve a low void percentage on the laminate. After the lay-up procedure completed, thermocouples and valves are located on the vacuum bag. Before putting the vacuum bags into the

autoclave, vacuum is applied to check leaks. The vacuum bag must not leak more than $25mmHg/Minute$. After the check is completed, the vacuum bags put into the autoclaves. Pressure is applied to the autoclave. Then, heat applied after full pressurization of the autoclave. According to cure cycles rates, heated up and cooled down. After the cure cycle completed, when temperature goes below $60°C$, vacuum and pressure are released. It should be noted that, unnotched specimen manufacturing involves two step curing. Firstly, the unnotched specimens and tabs cured separately. Then, the tabs are bonded to the unnotched specimens by using FM300K.05 [32] and cured together. As a final step of the manufacturing process, ultrasonic inspection performed to all laminates after demoulding. Cure cycles of the notched and the unnotched specimens with the end tabs given in Figures 4.4, 4.5, 4.6 and 4.7.
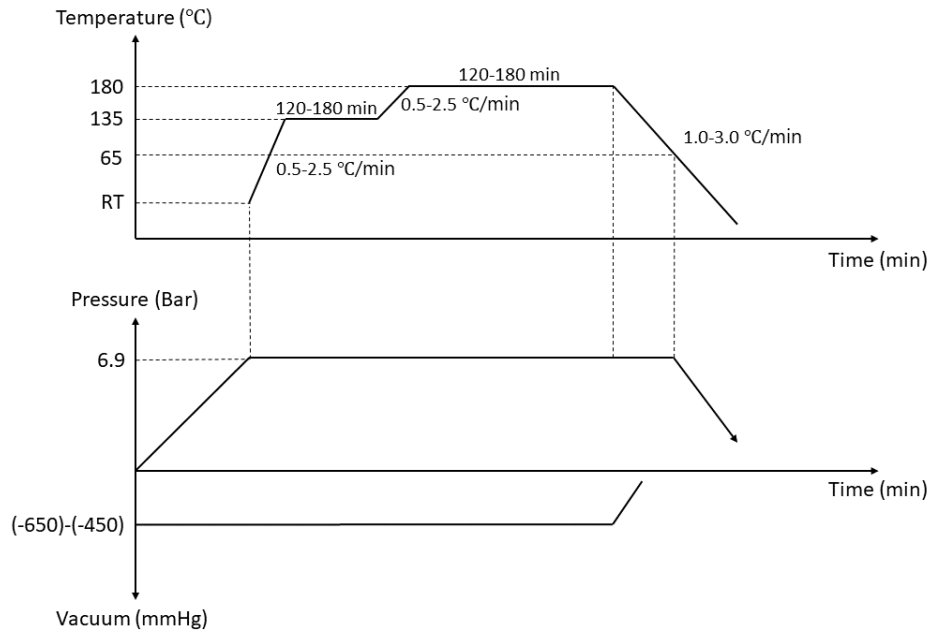
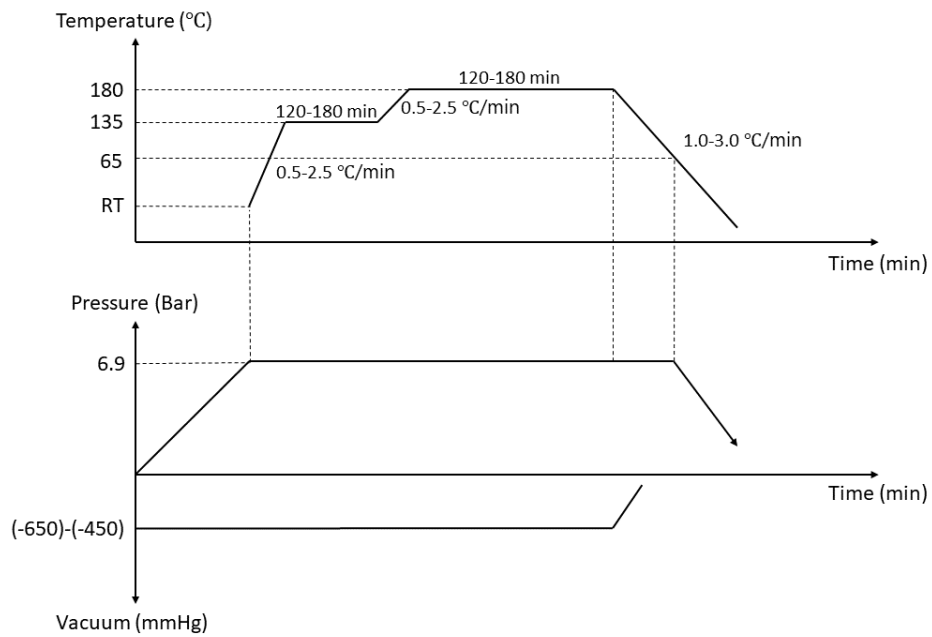Figure 4.4: Cure cycle graph of notched specimens.

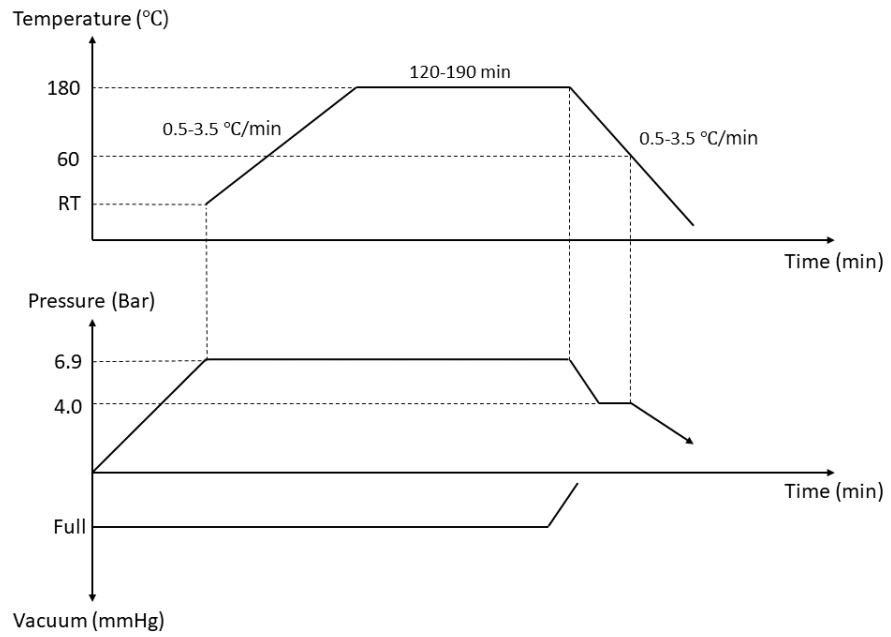Figure 4.5: Cure cycle graph of unnotched specimens.

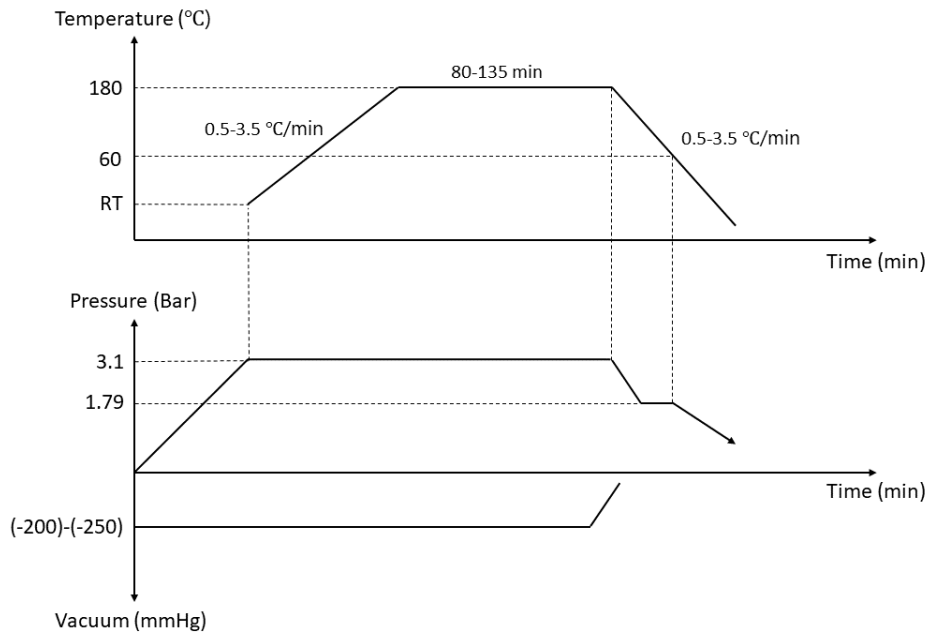Figure 4.6: Cure cycle graph of unnotched specimen tabs.

Figure 4.7: Cure cycle graph of unnotched specimens with tabs.

4.4 Specimen Preparation

4.4.1 Cutting and Drilling

Laminate plates are cut into the specimen sizes. As far as achievable, all test specimens for a certain testing condition are cut out from the same laminate plate. Deburring and breaking sharp edges of the specimen coupons are done.

4.4.2 Polishing

Side surface of the specimens are polished. This polishing is required to visualize initial damages on the specimen coupons. It also required to capture the high quality images from the high speed camera during the experiments. The specimen coupons are hand polished with a simple table setup.

Firstly, the specimen coupon clamped between two wooden blocks. Clamping force should not be too tight, otherwise it will damage the specimen coupon. Then, starting with grit size 400, polishing procedure is continued up to the grit size 4000. During the polishing, the surface of the specimen coupon wetted by spraying water. It helped to get smoother surface and get rid of any remaining particles.

4.4.3 Surface Painting

Top surface of every specimen is painted. This painting is required for the DIC studies. Firstly, the top surface is cleaned. Then, outside area of the DIC focus is covered with masking tape. White paint is applied as the base paint. Speckle pattern is generated using black paint on top of the white paint. The surface painting steps are shown in Figure 4.8.

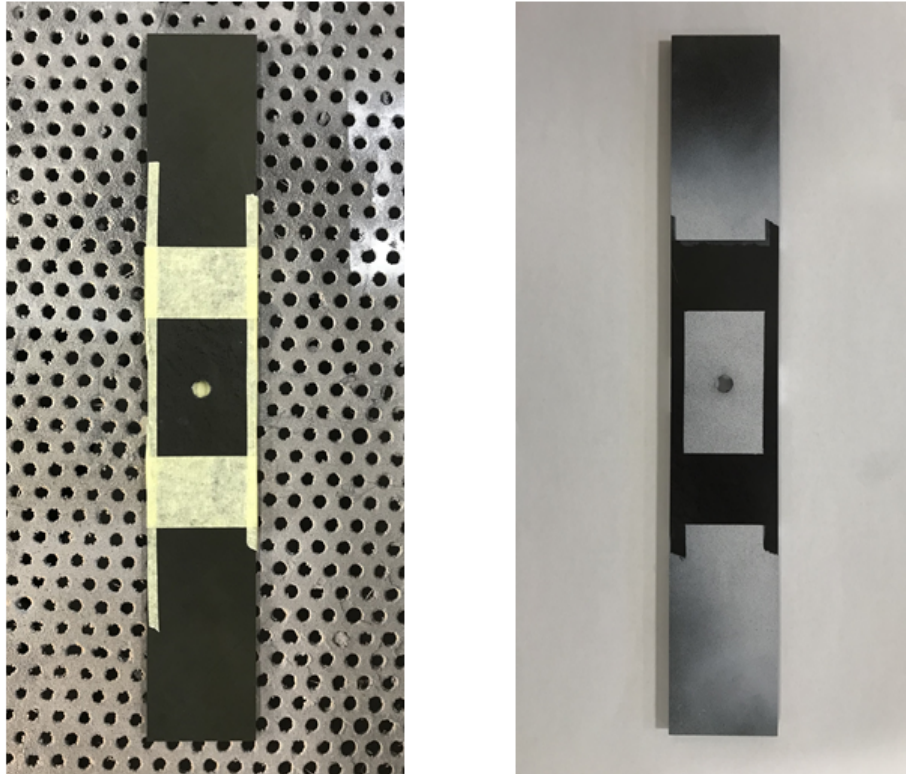Figure 4.8: The steps of surface painting.

4.5 Experimental Setup

The test specimen is clamped to the testing machine as shown in Figure 4.9. Two cameras are positioned and focused to the front and the side surfaces of the test specimen. External light sources are placed in order to get uniform luminosity on the specimen surfaces for high quality images.
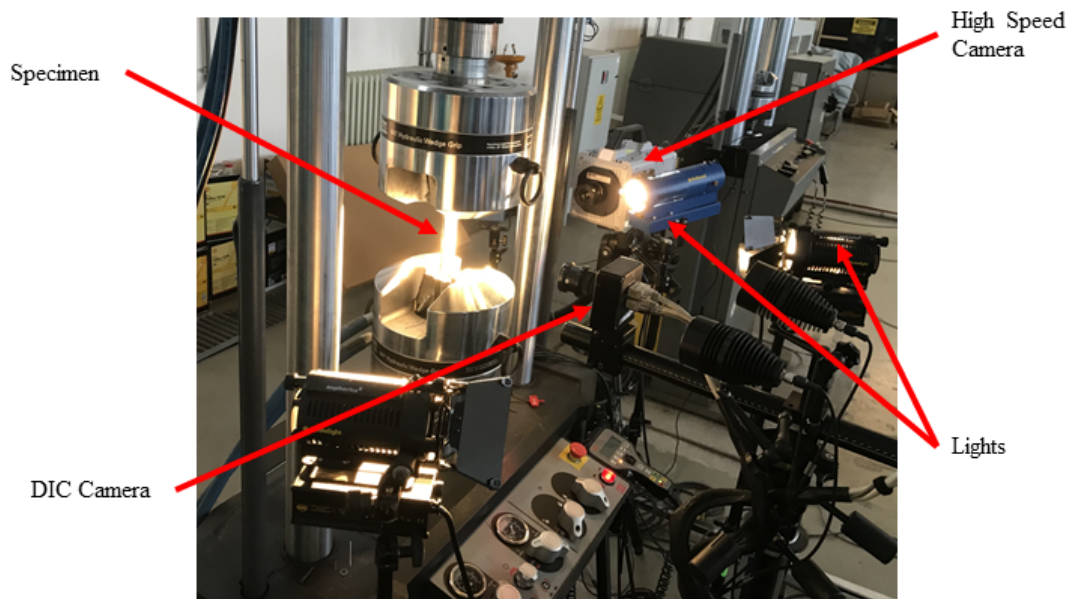

Figure 4.9: The Experimental set-up.

4.6 Experimental Procedure

Experimental procedure of this study can be examined in two phases. The first phase comprised preparation steps of the test specimen. These were marking of clamping regions and hole center, focusing the cameras and starting of the test. The second phase involved image capturing of failure, data acquisition and autopsy of the test specimen.

Prior to each experiment for each of the test specimens, the clamping locations and the hole center are marked. Then, the test specimen put into the test fixture and clamped. Once the test specimen clamped, camera sets are focused to the top and the side surface of the test specimen. The Experiments conducted on displacement controlled environment. Fixture head displacement rate set to $2mm/min$ according to suggestion given in ASTM standard[30]. High speed and high resolution cameras activated with the onset of experiment. When cracking sound of a failure is heard, the cameras are stopped with a trigger button. With the help of software before and after images of the test specimen are obtained.

During the experiments, in-situ data are acquired directly from the testing machine and the high speed and high resolution camera systems. The testing machine is recorded the load-displacement data throughout the experiments. The two different camera are focused on the top and the side surface of the test specimens. The top surface images of the test specimens are captured by using GOM-Aramis/Pontos camera system throughout the experiments. The image capturing process is started at the same time with the tensile test. The top surface images are used on DIC technique. The side surface images of the test specimens are captured by using High Speed Imaging PHOTRON SA-5X camera system. At the beginning of the tests, the high speed images are being stored on cache memory of the system. When the cracking sound of a failure is heard, trigger button is activated. With trigger signal, cache memory images of before and after the failure are transferred to main memory. The side surface images are used to determine failure mechanism.

After the experiments, each of the tested specimens are unclamped from the test fixture carefully. Post mortem images of the tested specimens are taken and detailed

examination is conducted by using HUVITZ HDS-5800 Digital Microscope. From the autopsy images, delamination and matrix cracks of the tested specimens can be observed.

4.7 Digital Image Correlation Method

Digital image correlation is a contact free optical technique for surface deformation and motion measurement. The idea behind DIC technique is the matching images before and after deformation. To tracking reference and current images, surface preparation is needed. As explained in Section 4.4.3, speckle pattern should be generated on the surface. To implement DIC method, the reference image should be divided into small subsets. The subset and deformation illustrations shown in Figures 4.10 and 4.11 [33].
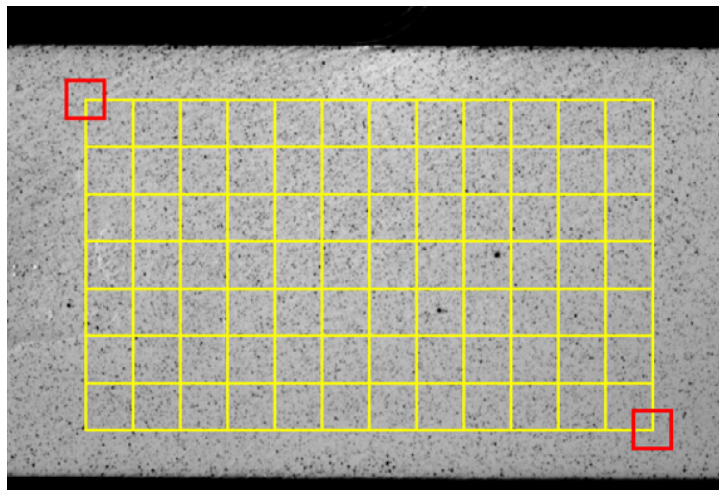
Figure 4.10: Virtual subsets on the region of interest [33].

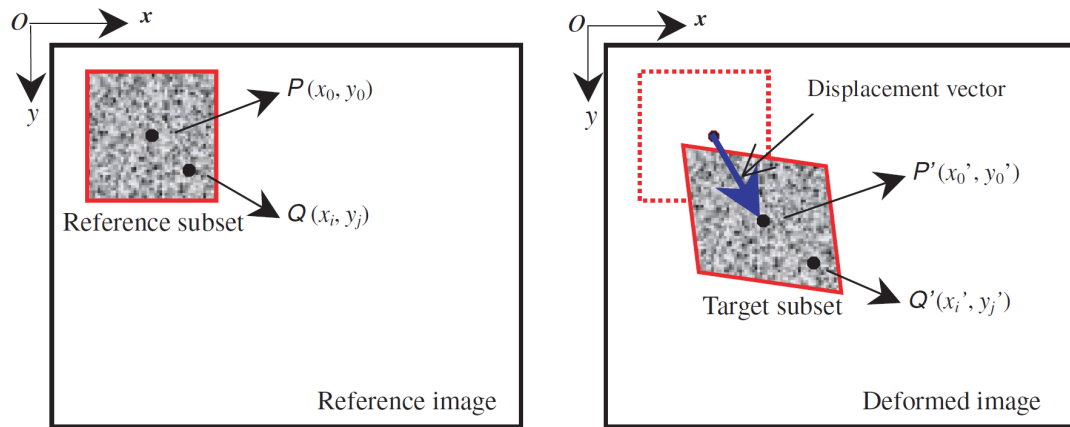Figure 4.11: Illustration of subset deformation [33].

In this study, the DIC technique is used to get surface strains of the test specimens throughout the experimental procedure. To capture images for the DIC technique, GOM-Aramis/Pontos camera system is used. After the experiments, captured top surface images processed using NCorr open-source 2D Digital image correlation Matlab software [34].

CHAPTER 5

RESULTS AND DISCUSSIONS

Results of the experiments and the proposed analytical methodology are given in following sections.

5.1 Experimental Results

As stated in Chapter 4, in-situ data are acquired directly from the testing machine and the high speed and high resolution camera systems. In the following sections load displacement curves, high speed camera images of the failure and the DIC results are presented. The post mortem observations of the tested specimens are also made.

5.1.1 Load Displacement Curves

In Figure 5.1, the load displacement curves of the tested unnotched tensile(UNT) test specimens are shown. Geometrical properties of the UNT test specimens along with the failure load and stress levels are tabulated in Table 5.1.

The UNT test specimens are prepared identical in terms of the width and the length. Only stacking sequence is varied between specimens. As seen in Figure 5.1, the failure load levels are proportionally increased with increase in the thickness. On all the UNT test specimens non-linearity is observed. As stated in Sadeghian comprehensive study [35], it can be explained with the presence of off-axis plies. During loading of the test specimens UNT2-1-1 and UNT3-1-1, slippage and small cracks are occurred on the tab locations. That can be observed as load drops on the load displacement curves of the specimens. Brittle failure is observed on all of the tested specimens.
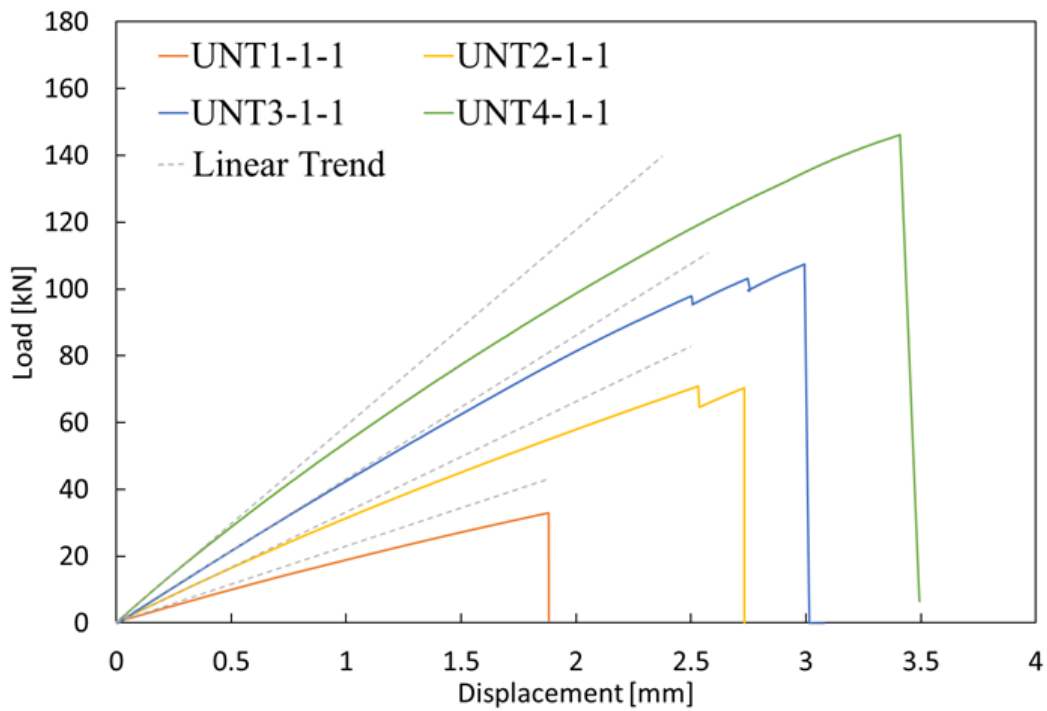
Figure 5.1: Load displacement curves of UNT test specimens.

Table 5.1: UNT test results.

Specimen	Thickness $t\,(mm)$	Width $w\,(mm)$	Failure Load $F\,(kN)$	Failure Stress $\sigma\,(MPa)$
UNT1-1-1	1.53	25.07	32	843
UNT2-1-1	2.95	25.08	71	958
UNT2-1-2	2.96	25.09	73	985
UNT2-1-7	2.99	25.05	72	964
UNT3-1-1	4.41	24.99	107	974
UNT3-1-2	4.44	25.02	116	1047
UNT3-1-3	4.39	25.06	107	970
UNT4-1-1	5.91	25.00	146	990

On the OHT tests, the effects of the thickness and the hole size are examined. Geometrical properties of the OHT test specimens along with the failure load and stress levels are tabulated in Table 5.2. The specimen OHT4-4-1 is tested but the failure load level cannot achieved and the specimen cannot be broken. Therefore, its results are excluded on this study. Load displacement curves of each tested specimen are given in Appendix C.

Table 5.2: The OHT test results.

Specimen	Thickness t (mm)	Hole Size ϕ (mm)	Width w (mm)	Failure Load F_N (kN)	Failure Stress σ_N (MPa)
OHT1-1-1	1.52	3.20	19.15	17	595
OHT2-1-1	2.99	3.25	19.00	36	641
OHT2-2-1	2.97	4.80	29.09	49	568
OHT2-2-7	2.88	4.82	29.03	49	580
OHT2-3-7	3.03	6.34	38.07	59	511
OHT2-4-7	2.96	12.67	76.15	107	473
OHT2-5-7	2.91	25.38	152.42	187	422
OHT3-1-1	4.41	3.19	19.09	53	630
OHT3-2-1	4.44	4.84	28.99	71	552
OHT3-2-2	4.45	4.82	29.01	73	564
OHT3-2-3	4.47	4.84	28.99	74	572
OHT3-3-1	4.43	6.36	38.11	91	542
OHT3-3-2	4.44	6.36	38.16	92	540
OHT3-3-3	4.50	6.37	38.11	91	531
OHT3-4-1	4.43	12.60	76.26	167	495
OHT4-1-1	5.80	3.18	19.06	68	619
OHT4-4-1	5.90	12.63	76.35	N/A	N/A

The failure stress levels needed to be compared to understand the size effects on the tested specimens. The tested specimens are examined in groups to observe the size effects on the failure stress levels. First group had the same hole sizes and varying thicknesses. The thickness effect can be examined from the results of this group. Second group had same the thicknesses and varying hole sizes. The hole size effect

can be examined from the results of this group. In Figure 5.2, results of the tested specimens along with the hole size and thickness properties are given.
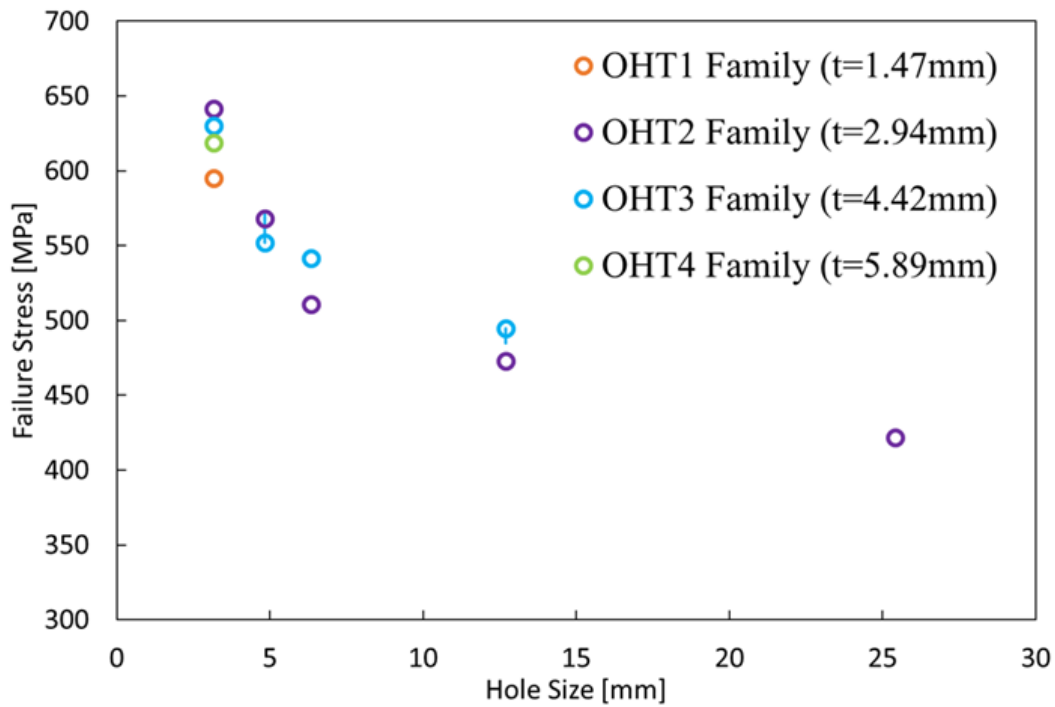

Figure 5.2: Comparison of failure stresses of the OHT test specimens.

Notched strength of the open hole composite laminates decreases with increase in hole size. Difference in notched strengths are getting smaller as the hole size increases. This can be explained with sub-critical damage phenomena [23]. The sub-critical damage delaying the onset of failure. As the hole size increases, the sub-critical damage decreases. Therefore, stress redistribution due to the sub-critical damage cannot be accomplished.

5.1.2   In-Situ and Post Mortem Observations

In order to find best setup to catch crack progress on the OHT specimens, an optimization study is conducted. The most critical part of the capturing high speed camera images is to find ideal frame-per-second(fps) and resolution combination. As the fps increases, possibility to catch crack progress increases. On the other hand, the resolution decreases with increase in the fps. Thus, capturing area decreases. By virtue of that, crack progress may not be fully captured. Also, effect of surface paint on visualization is studied. However, it is not possible to determine exact plies on the images due to the surface paint. Therefore, post mortem examination of the tested specimens on microscope is a must. In this section, detailed examination of OHT3-2-1, OHT3-2-2, OHT3-3-1 and OHT3-3-2 are given. Results of the other specimens are given in Appendix C.
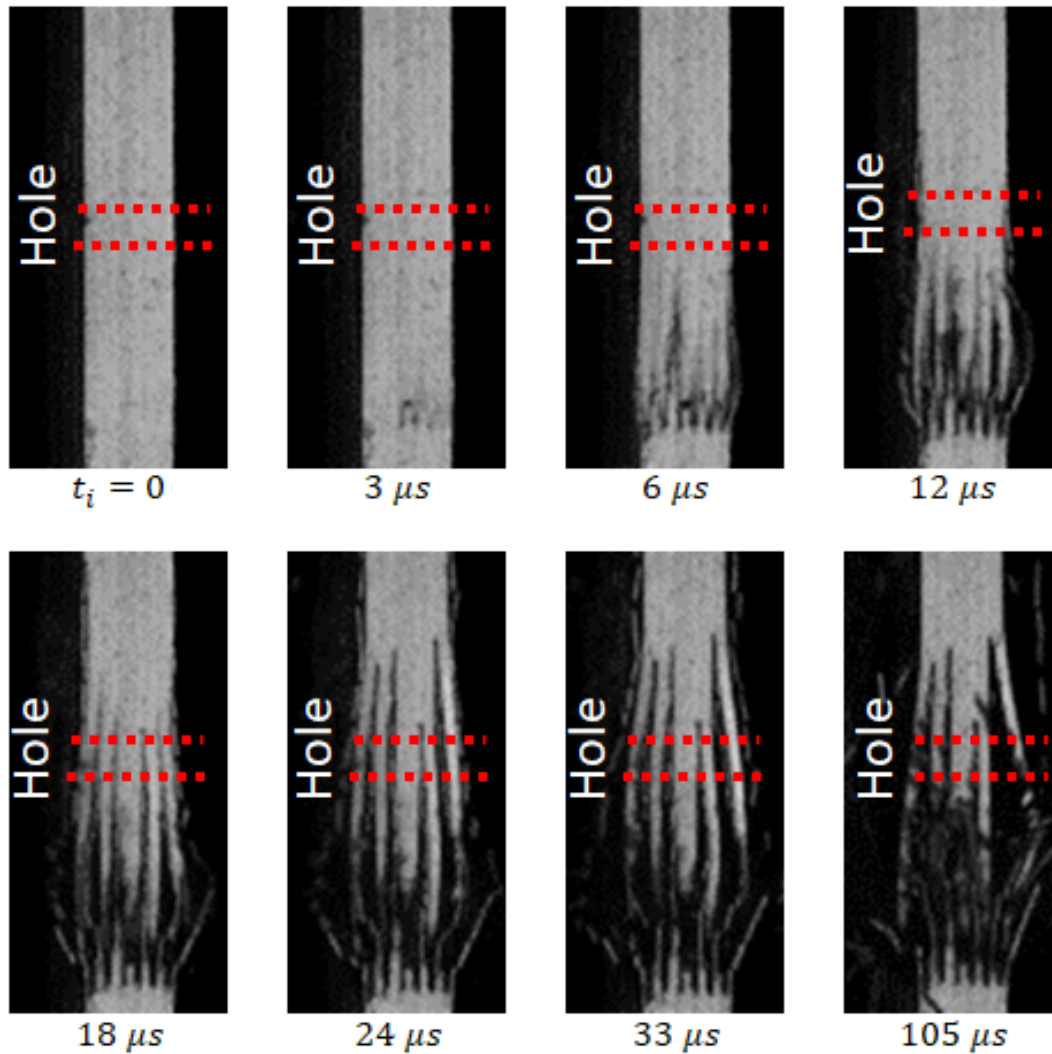
OHT3-2-1

Figure 5.3: High speed camera images of the OHT3-2-1 test specimen at 325500 fps.

Experiment is conducted at 325500 fps with 64 x 136 pixels resolution on the test specimen OHT3-2-1. In Figure 5.3, sequential images of the failure are shown. Red dashed lines correspond to hole edges. On this experiment, specimen side surface is painted with white color for better visualization of the crack progress. First crack is observed on the side surface of the specimen within $3\mu s$. These cracks expanded through the specimen thickness. Once the cracks reached the top and bottom surfaces of the specimen delamination of plies is observed.
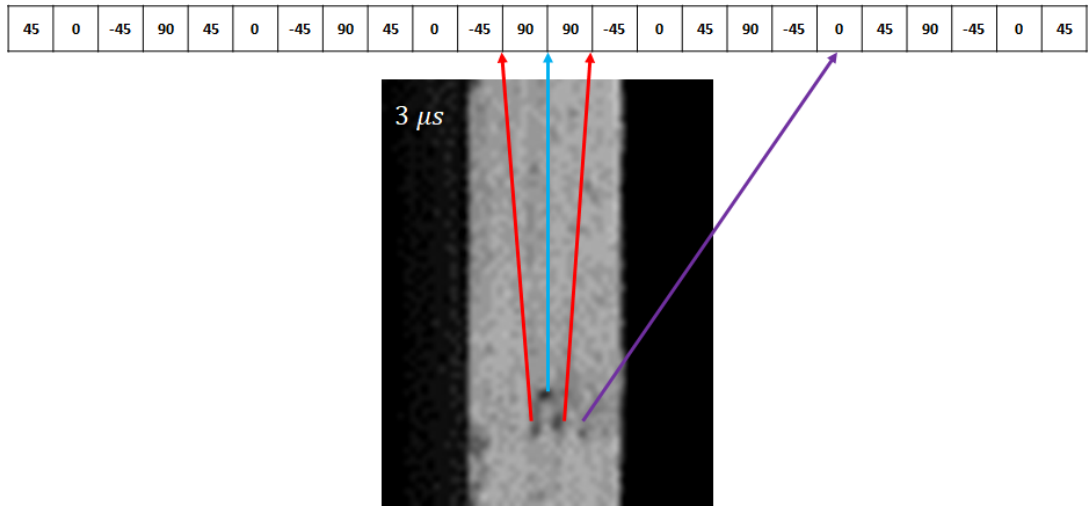
45	0	-45	90	45	0	-45	90	45	0	-45	90	90	-45	0	45	90	-45	0	45	90	-45	0	45

Figure 5.4: Crack initiation on the OHT3-2-1 test specimen.

As it can be seen in Figure 5.4, cracks are observed on $-45°/90°$ interface and $0°$, $90°$ plies.
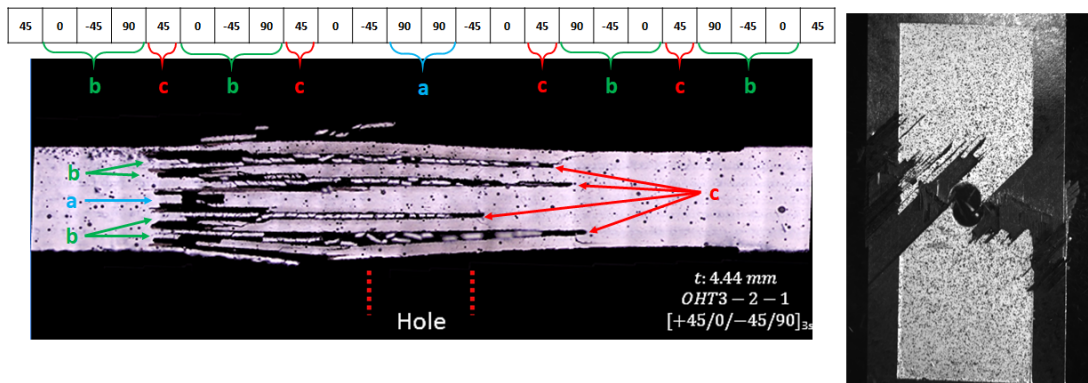

Figure 5.5: Post mortem image of the OHT3-2-1 test specimen at 50x magnification.

In Figure 5.5, post mortem image of the specimen OHT3-2-1 is shown. Extensive matrix cracks accompanied with small deleminations are observed on off-axis plies. Damage propagation is contained by $0°$ plies. Total failure throughout the thickness of the specimen is observed away from the hole where $45°$ plies are tangential to the hole edge.
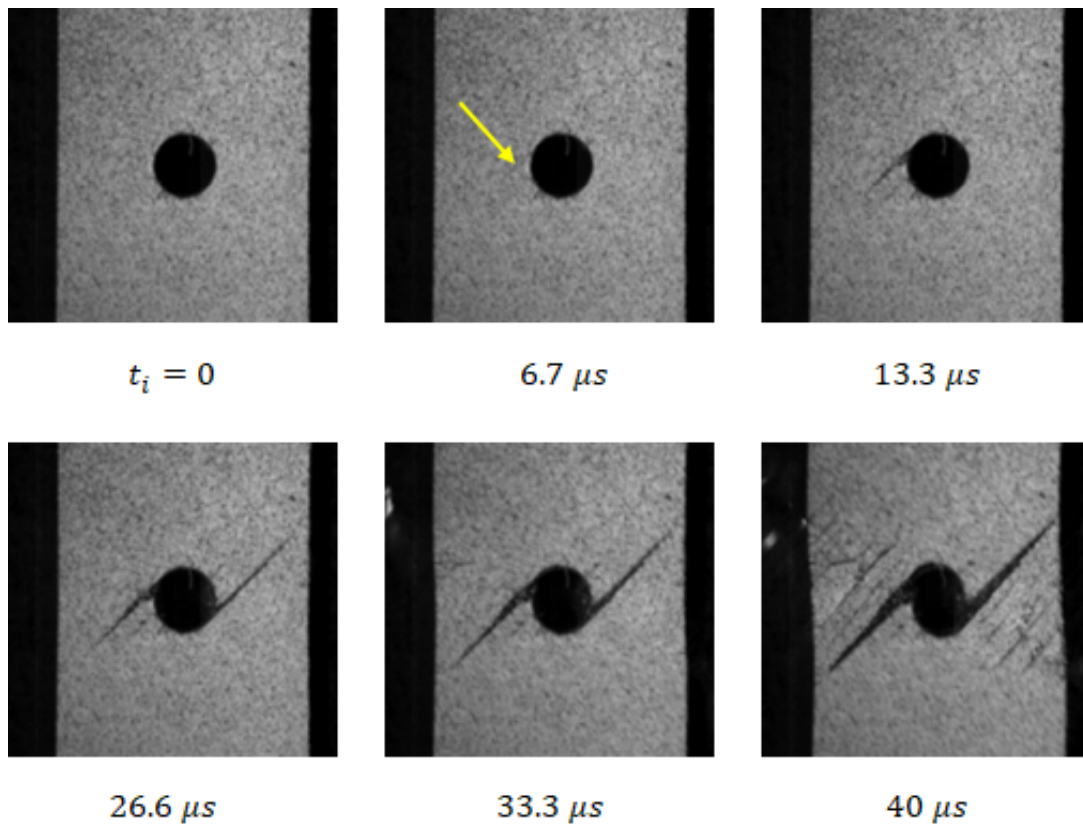
OHT3-2-2

Figure 5.6: High speed camera images of the OHT3-2-2 test specimen at 150000 fps.

Experiment is conducted at 150000 fps with 192 x 184 pixels resolution on the test specimen OHT3-2-2. In Figure 5.6, sequential images of the failure are shown. First crack is observed on top surface of the specimen within 6.7 μs. First two cracks are tangential to hole and along the $45°$. Within 40 μs, cracks are expanded along the width of the specimen on a $-45°$ direction.
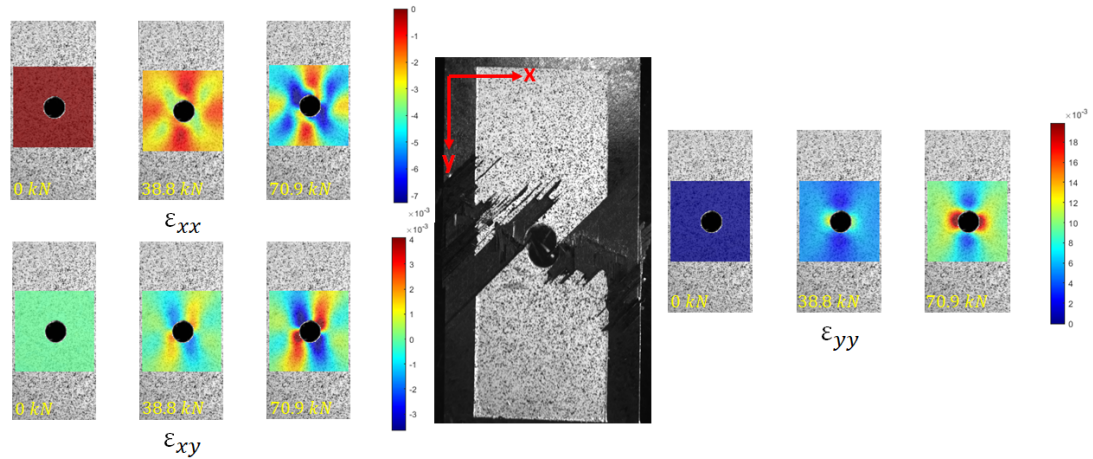
Figure 5.7: Change of strain distribution on the OHT3-2-2 test specimen up to the failure.

In Figure 5.7, DIC results in terms of strain plots ε_{xx} (transverse direction), ε_{yy} (loading direction) and ε_{xy} of the test specimen OHT3-2-2 up to the failure are shown. In the DIC strain images, high localized strain levels are observed near the hole region. The high localized longitudinal and shear strains are introduced matrix cracks near the hole region. These matrix cracks are accumulated and sub-critical damage zone is occurred near the hole region. The propagation path can be inferred by looking the shear strain distribution. Strain concentrations can be observed in the ε_{xy} at the hole edge where $45°$ plies are tangential. Also, small strain concentrations can be observed away from the hole edge and still tangent to $45°$ plies.
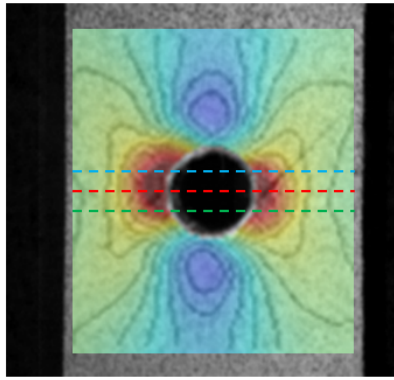
$DIC\ at\ t_i = 0$

$In - situ\ image\ at\ t = 26.6\ \mu s$
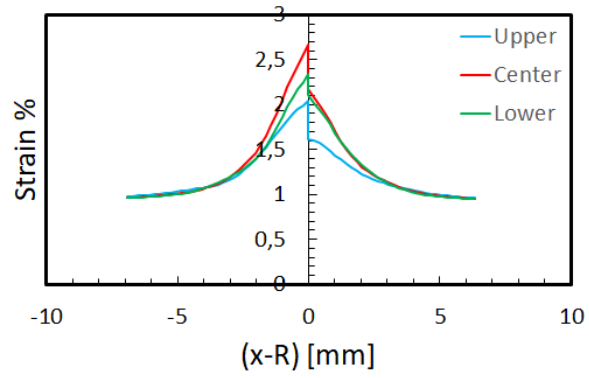
ε_{yy}

Figure 5.8: Strain field and strain plot along the paths shown by dashed lines.

Strain field and strain plots just before the failure are given Figure 5.8. Strains are plotted on three different lines. One along the center of the hole and two of them just above and below the center line. Higher strain rates are observed on the left side of the hole. That supports the first crack initiation location on the surface of the specimen.

OHT3-3-1

$t_i = 0$ 1.7 μs 3.4 μs 5.1 μs

6.8 μs 11.9 μs 17 μs 105.4 μs
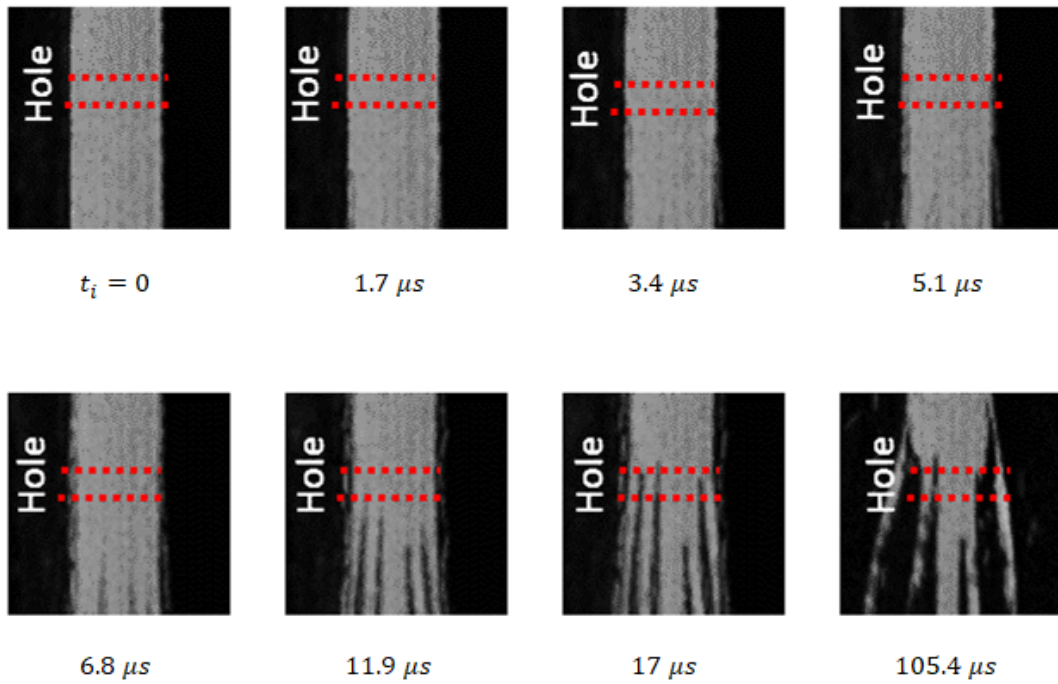
Figure 5.9: High speed camera images of the OHT3-3-1 test specimen at 581250 fps.

Experiment is conducted at 581250 fps with 64 x 64 pixels resolution on the test specimen OHT3-3-1. In Figure 5.9, sequential images of the failure are shown. Red dashed lines correspond to hole edges. On this experiment, failure progression is captured. However, due to small resolution starting area of the failure cannot be captured. Firstly, in the focused area, outermost plies are splitted. Starting point of the damage mechanism cannot be seen due to captured area limitation. Then, damage progressed on the inner plies. Also, it should be noted that outer damage goes faster than the inner ones. At the last image, final failure of the specimen is observed. Damaged plies are accumulated and damage propagated throughout the width of the specimen.
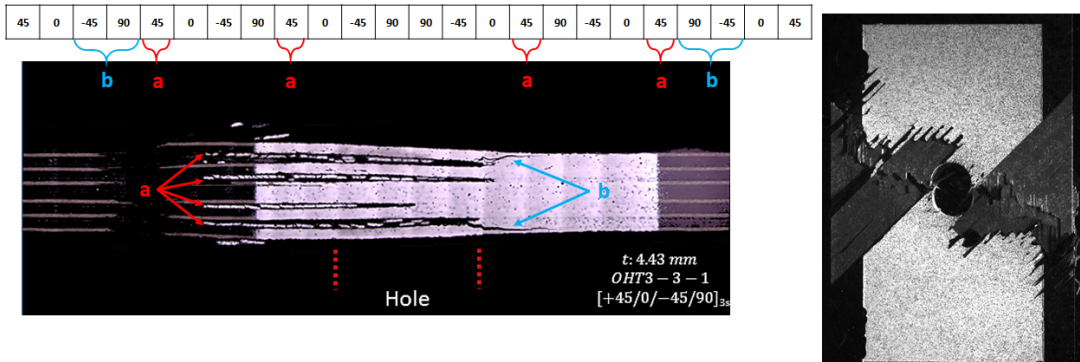
Figure 5.10: Post mortem image of the OHT3-3-1 test specimen at 50x magnification.

In Figure 5.10, post mortem image of the specimen OHT3-3-1 is shown. Extensive amount of matrix cracks are observed on the off-axis plies. The matrix cracks are followed by delaminations and plies are isolated. On the right side, two cracks on $-45°/90°$ interface near to the top and the bottom surfaces of the specimen can be observed. Total failure throughout the thickness of the specimen is observed away from the hole on the left side where $45°$ plies are tangential to the hole edge.

OHT3-3-2

$t_i = 0$ 6.7 μs 13.3 μs

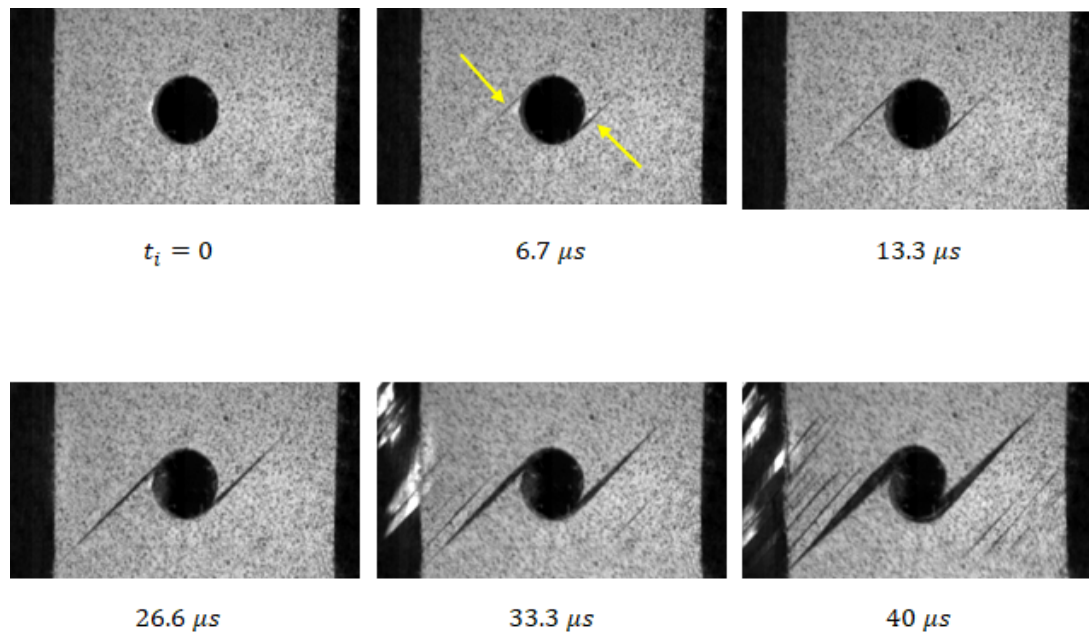26.6 μs 33.3 μs 40 μs

Figure 5.11: High speed camera images of the OHT3-3-2 test specimen at 150000 fps.

Experiment is conducted at 150000 fps with 256 x 144 pixels resolution on the test specimen OHT3-3-2. In Figure 5.11, sequential images of the failure are shown. Two symmetrical cracks are observed on top surface of the specimen within 6.7 μs. These cracks are tangential to hole and along the $45°$. Within 40 μs, cracks are expanded along the width of the specimen on a $-45°$ direction.
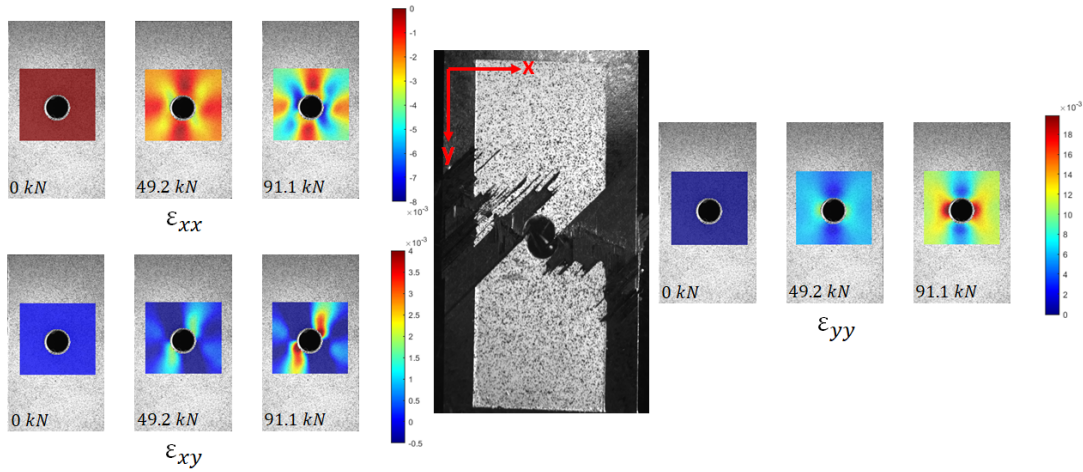
Figure 5.12: Change of strain distribution on the OHT3-3-2 test specimen up to the failure.

In Figure 5.12, DIC results in terms of strain plots ε_{xx} (transverse direction), ε_{yy} (loading direction) and ε_{xy} of the test specimen OHT3-3-2 up to the failure are shown. Similar to the test specimen OHT3-2-2, high localized strain levels are observed near the hole region. The propagation path can be inferred by looking the shear strain distribution. Strain concentrations can be observed in the ε_{xy} at the hole edge where $45°$ plies are tangential. Again, small strain concentrations can be observed away from the hole edge and still tangent to $45°$ plies.
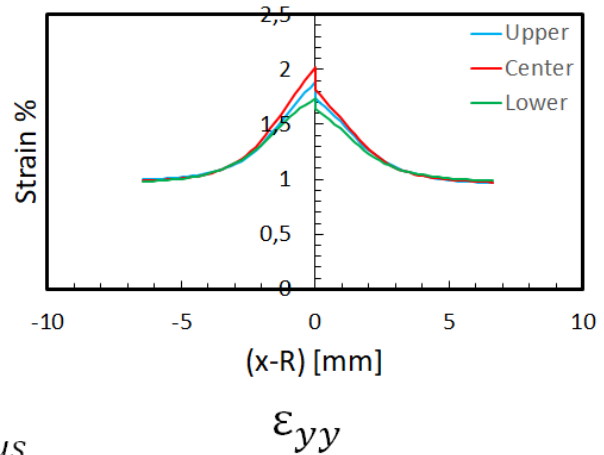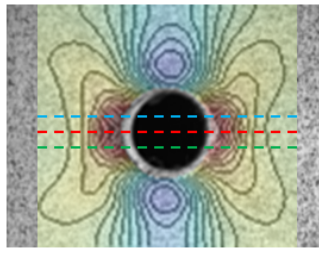
DIC at $t_i = 0$

In $-$ situ image at $t = 6.7\ \mu s$

ε_{yy}

Figure 5.13: Strain field and strain plot along the paths shown by dashed lines.

Strain field and strain plots just before the failure are given Figure 5.13. Strains are plotted on three different lines. One along the center of the hole and two of them just above and below the center line. Strain rates on both side of the hole are close. That supports the symmetrical crack initiation on the surface of the specimen. Also, lower strain rates are observed compared to the OHT3-2-2 specimen.

Outcome of these test shows that, cracks are initiated on off-axis plies. These cracks then followed by the delaminations on $0°$ interfaces. Damage propagation is delayed by $0°$ plies. Through the thickness failure is observed away from the hole center. That location is where the off-axis plies are tangential to the hole. The matrix cracks are initiated at the hole edge and continued up to the edge of the specimen where the hole edge is tangential to the $45°$.Then, damage is initiated rest of the plies and pull-out failure is occurred.

5.2 Analytical Results

Three different analytical approaches are used. As explained throughout this study, these are the point stress criterion(PSC), average stress criterion(ASC) and extended point stress methodology(EPSM). Characteristic distance values are determined based on UNT2 and OHT2 specimen families. The reason of that is all hole sizes are covered in this set. For the analytical approaches, using Eqs. (2.4), (2.5) and (3.2), the characteristic distance values and the notch sensitivity factor are found as

$$d_0 = 0.87mm \quad , \quad a_0 = 2.11mm \quad , \quad n = 0.3$$

Analytical results of the tested specimens by using EPSM, PSC and ASC are given in following tables and figures.

Table 5.3: The analytical results of PSC, ASC and EPSM approaches.

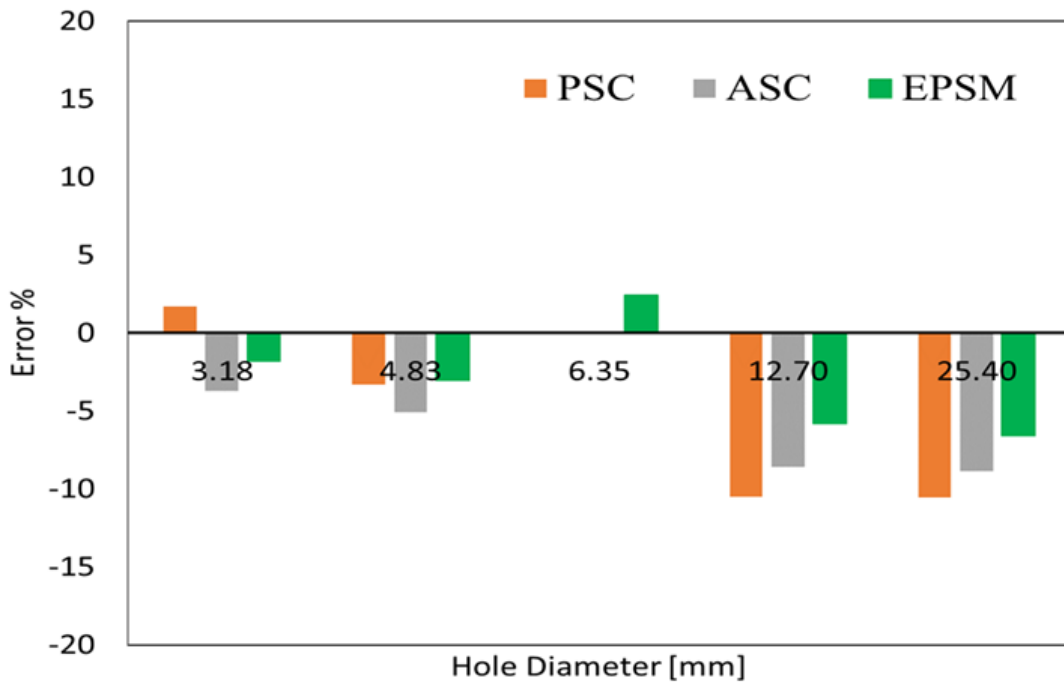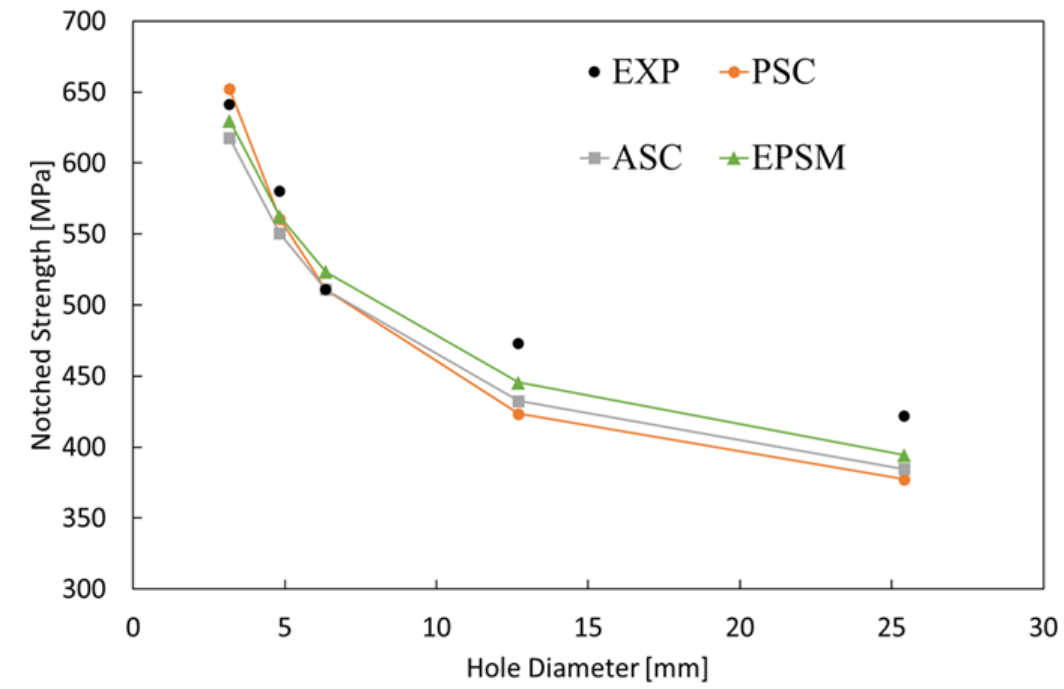| Specimen	σ_N (MPa) Experimental	σ_N (MPa) PSC	Error(%) PSC	σ_N (MPa) ASC	Error(%) ASC	σ_N (MPa) EPSM	Error(%) EPSM
OHT1-1-1	595.28	573.28	−3.70	540.14	−9.26	629.82	+5.80
OHT2-1-1	641.30	652.12	+1.69	617.55	−3.70	629.81	−1.79
OHT2-2-1	568.05	560.82	−1.27	550.59	−3.07	562.39	−1.00
OHT2-2-7	580.03	560.82	−3.31	550.59	−5.08	562.39	−3.04
OHT2-3-7	511.02	511.02	N/A	511.02	N/A	523.46	+2.43
OHT2-4-7	473.10	423.46	−10.49	432.41	−8.60	445.63	−5.81
OHT2-5-7	422.04	377.48	−10.56	384.67	−8.85	394.32	−6.57
OHT3-1-1	630.35	662.13	+5.04	623.85	−1.03	629.82	−0.08
OHT3-2-1	551.95	569.67	+3.21	555.82	+0.70	562.39	+1.89
OHT3-2-2	563.66	569.67	+1.07	555.82	−1.39	562.39	−0.22
OHT3-2-3	572.13	569.67	−0.43	555.82	−2.85	562.39	−1.70
OHT3-3-1	541.62	518.41	−4.29	515.38	−4.85	523.46	−3.35
OHT3-3-2	539.85	518.41	−3.97	515.38	−4.53	523.46	−3.04
OHT3-3-3	531.42	518.41	−2.45	515.38	−3.02	523.46	−1.50
OHT3-4-1	494.78	426.19	−13.86	434.06	−12.27	445.63	−9.93
OHT4-1-1	618.89	672.96	+8.74	634.06	+2.45	629.82	+1.77

Figure 5.14: Comparison of experimental and analytical results of OHT2 family specimens.
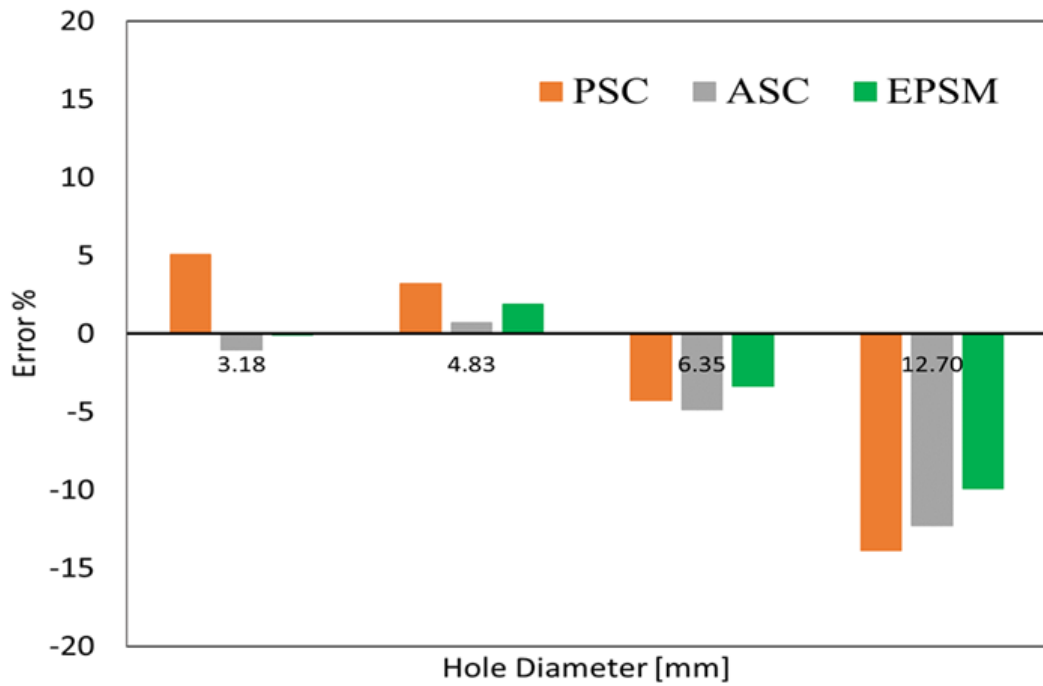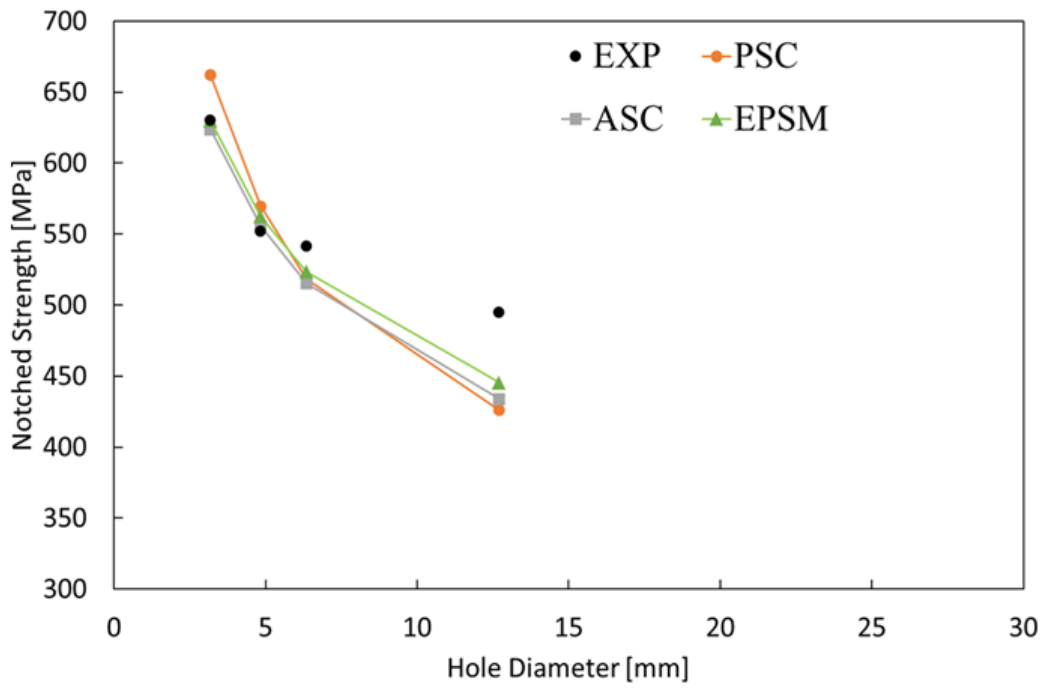
Figure 5.15: Comparison of experimental and analytical results of OHT3 family specimens.

In table 5.3, for the OHT2-3-7 named test specimen error percentages for PSC and ASC methodologies are shown as N/A. This specimen used as reference for the characteristic distance calculations. Therefore, this is meaningless to shown it as perfect match. As it can be seen on Figure 5.14 and Figure 5.15, good correlation is achieved, for all of the analytical methodologies, with the experimental results.

Trend of notched strength levels with varying hole thicknesses is captured. In smaller hole sizes, the analytical results showed very small error, up to 5%. As the hole sizes goes beyond $6.35mm$, error levels drastically increase. It can be explained with the nature of the characteristic distance phenomena. In the basis, determination of the characteristic distance is based on the curve fitting of the experimental results. At the extremum points, smallest and largest hole sizes, it is normal to have higher error levels. Almost every case, the EPSM is shown better match compared to the PSC and the ASC methodologies.

CHAPTER 6

CONCLUSIONS

In this work, effect of size on the notched strength of a quasi-isotropic composite laminates with a hole subjected to uniaxial monotonic tensile loading is studied using experimental and analytical approaches.

In order to investigate the size effect on the strength of open hole composite laminates:

- Tensile test experiments on $[+45/0/-45/90]_{ns}$ CFRP open hole composite specimens are conducted.

  - Sublaminate-scaling is used to increase thickness of specimens.
  - Width to diameter ratio is kept constant on all specimens.

- In-situ data acquired directly from the testing machine and the high speed and high resolution camera systems during the experiments.

  - Failure sequence of the open hole composite laminates under tensile loading is captured using high-speed camera system. First cracks are observed on $-45/90$ interfaces and $0°$ plies.
  - On the side surface, cracks are expanded through the specimen width away from the hole region.
  - Pull-out failure mechanism is observed on all specimens.
  - Notched strength of the open hole composite laminates decreases with increase in the hole size, consistent with the literature.

- Tested specimens are studied under the microscope.

    - Extensive amount of matrix cracks are observed on the off-axis plies.

    - Damage propagation is contained by $0°$ plies.

    - Total failure through the thickness of the specimen is observed away from the hole where $45°$ plies are tangential to the hole edge.

- A new analytical methodology(EPSM) based on Tan's approach is developed and implemented into a code to predict notched strength of the open hole composite laminates.

    - Yamada Sun + Puck iterative failure criterion is used on Tan's approach for the first time.

    - The EPSM is shown better results compared to PSC and ASC methodologies in almost every test case.

    - The EPSM is required less tests compared to PSC and ASC methodologies. Necessity of unnotched test is eliminated.

REFERENCES

[1] N. V. Nayak, "Composite materials in aerospace applications," *International Journal of Scientific and Research Publications*, vol. 4, no. 9, 2014.

[2] International Renewable Energy Agency, "Status of faa's actions to oversee the safety of composite airplanes," September 2011.

[3] Airbus, "Flight trials begin to help optimise a350 xwb cabin sound insulation," February 2010. `www.airbus.com`.

[4] Boom Supersonic, "Wing spars: The backbone of xb-1's wings," February 2020. `blog.boomsupersonic.com`.

[5] Federal Aviation Administration, "Composite aircraft structure," September 2009.

[6] J. Awerbuch and M. S. Madhukar, "Notched strength of composite laminates: Predictions and experiments: A review," *Journal of Reinforced Plastics and Composites*, vol. 4, no. 1, pp. 3–159, 1985.

[7] M. N. Nahas, "Survey of failure and post-failure theories of laminated fiber-renforced composites," *Journal of Composites Technology and Research*, vol. 8, no. 4, pp. 138–153, 1986.

[8] M. E. Waddoups, J. R. Eisenmann, and B. E. Kaminski, "Macroscopic fracture mechanics of advanced composite materials," *Journal of Composite Materials*, vol. 5, no. 4, pp. 446–454, 1971.

[9] O. L. Bowie, "Analysis of an infinite plate containing radial cracks originating at the boundary of an internal circular hole," *Journal of Mathematics and Physics*, vol. 35, no. 4, pp. 60–71, 1956.

[10] J. M. Whitney and R. J. Nuismer, "Stress fracture criteria for laminated composites containing stress concentrations," *Journal of Composite Materials*, vol. 8, no. 3, pp. 253–265, 1974.

[11] S. Timoshenko and J. N. Goodier, *Theory of elasticity. (2nd edition).* McGraw Hill Book Company, 1951.

[12] S. C. Tan, *Stress Concentrations in Laminated Composites.* Lancaster: Technomic Pub. Co., 1994.

[13] R. F. Karlak, "Hole effects in a related series of symmetrical laminates," in *Proceedings of Failure Modes in Composites, IV.,*, pp. 105–117, The Metallurgical Society of AIME, Chicago, 1977, 1977.

[14] R. B. Pipes, R. C. Wetherhold, and J. W. Gillespie, "Notched strength of composite materials," *Journal of Composite Materials*, vol. 13, no. 2, pp. 148–160, 1979.

[15] H. J. Konish and J. M. Whitney, "Approximate stresses in an orthotropic plate containing a circular hole," *Journal of Composite Materials*, vol. 9, no. 2, pp. 157–166, 1975.

[16] S. C. Tan, "Notched strength prediction and design of laminated composites under in-plane loadings," *Journal of Composite Materials*, vol. 21, no. 8, pp. 750–780, 1987.

[17] S. C. Tan, "Mixed-mode fracture of notched composite laminates under uniaxial and multiaxial loading," *Engineering Fracture Mechanics*, vol. 31, no. 5, pp. 733–746, 1988.

[18] T. A. Cruse, "Tensile strength of notched composites," *Journal of Composite Materials*, vol. 7, no. 2, pp. 218–229, 1973.

[19] T. A. Cruse, "Tensile fracture of composites with circular holes," *Materials Science and Engineering*, vol. 41, no. 1, pp. 121–125, 1979.

[20] P. A. Lagace, "Notch sensitivity and stacking sequence of laminated composites," *Composite Materials: Testing and Design (Seventh Conference), ASTM STP 893.* J. M. Whitney, Ed., American Society for Testing and Materials, Philadelphia, pp. 161-176, 1986.

[21] C. E. Harris and D. H. Morris, "Role of delamination and damage development on the strength of thick notched laminates," *Delamination and Debonding of*

Materials, ASTM STP 876. W. S. Johnson, Ed., American Society for Testing and Materials, Philadelphia, pp. 424-447, 1985.

[22] C. E. Harris and D. H. Morris, "Effect of laminate thickness and specimen configuration on the fracture of laminated composites," *Composite Materials: Testing and Design (Seventh Conference), ASTM STP 893.* J. M. Whitney, Ed., American Society for Testing and Materials, Philadelphia, pp. 177-195, 1986.

[23] B. G. Green, M. R. Wisnom, and S. R. Hallett, "An experimental investigation into the tensile strength scaling of notched composites," *Composites Part A: Applied Science and Manufacturing*, vol. 38, no. 3, pp. 867–878, 2007.

[24] S. E. Yamada and C. T. Sun, "Analysis of laminate strength and its distribution," *Journal of Composite Materials*, vol. 12, no. 3, pp. 275–284, 1978.

[25] A. Puck, "Festigkeitsberechnung an glasfaser/kunststoff-laminaten bei zusammengesetzter beanspruchung," *Kunststoffe*, vol. 59, no. 11, pp. 780–787, 1969.

[26] A. Puck and W. Schneider, "On failure mechanisms and failure criteria of filament-wound glass-fiber/resin composites," *Plastic and Polymer Technology*, vol. 37, pp. 33–43, 1969.

[27] M. Knops, *Analysis of Failure in Fiber Polymer Laminates:The Theory of Alfred Puck.* Springer, 2008.

[28] Hexcel, *Hexply® M91 Product Data Sheet*, 2020. www.hexcel.com.

[29] R. Bogenfeld, J. Kreikemeier, and T. Wille, "Review and benchmark study on the analysis of low-velocity impact on composite laminates," *Engineering Failure Analysis*, vol. 86, pp. 72–99, 2018.

[30] ASTM D3039/D3039M-17, *Standard Test Method for Tensile Properties of Polymer Matrix Composite Materials*, ASTM International, West Conshohocken, PA, 2017. www.astm.org.

[31] ASTM D5766/D5766M-11(2018), *Standard Test Method for Open-Hole Tensile Strength of Polymer Matrix Composite Laminates*, ASTM International, West Conshohocken, PA, 2018. www.astm.org.

[32] Solvay, *Technical Data Sheet FM 300® Film Adhesive*, Solvay, Composite Materials HQ, GA, 2018. `www.solvay.com`.

[33] B. Pan, K. Qian, H. Xie, and A. Asundi, "Two-dimensional digital image correlation for in-plane displacement and strain measurement: a review," *Measurement Science and Technology*, vol. 20, no. 6, 2009.

[34] J. Blaber, B. Adair, and A. Antoniou, "Ncorr: Open-source 2d digital image correlation matlab software," *Experimental Mechanics*, vol. 55, 2009.

[35] P. Sadeghian, A. R. Rahai, and M. R. Ehsani, "Effect of fiber orientation on nonlinear behavior of cfrp composites," *Journal of Reinforced Plastics and Composites*, vol. 28, no. 18, 2009.

[36] S. G. Lekhnitskii, S. W. Tsai, and T. Cheron, *Anisotropic Plates*. New York: Gordon and Breach Science Publishers, 1968.

[37] A. C. Ugural and S. K. Fenster, *Advanced Mechanics of Materials and Elasticity*. Prentice Hall, 2012.

[38] P. Berbinau, C. Filiou, and C. Soutis, "Stress and failure analysis of composite laminates with an inclusion under multiaxial compression-tension loading," *Applied Composite Materials*, vol. 8, no. 5, pp. 307–326, 2001.

[39] T. Kundu, *Fundamentals of Fracture Mechanics*. CRC Press, 2008.

APPENDIX A

LEKHNITSKII COMPLEX VARIABLE MAPPING METHOD

This chapter is devoted to the explanation of the derivation of Lekhnitskii equations, which are used for the generation of stress fields in an orthotropic plate with an elliptical opening. According to Lekhnitskii, elastic equilibrium equations are satisfied by the introduction of an Airy stress function $F(x, y)$ [36]. In the absence of the body forces, these equations are

$$\overline{\sigma}_x = \frac{\partial^2 F}{\partial y^2} \qquad \overline{\sigma}_y = \frac{\partial^2 F}{\partial x^2} \qquad \overline{\tau}_{xy} = \frac{-\partial^2 F}{\partial x \partial y} \tag{A.1}$$

Condition of compatibility of deformation is [37]

$$\frac{\partial^2 \overline{\varepsilon}_x}{\partial y^2} + \frac{\partial^2 \overline{\varepsilon}_y}{\partial x^2} + \frac{\partial^2 \overline{\gamma}_{xy}}{\partial x \partial y} = 0 \tag{A.2}$$

For an anisotropic body, average strain values are

$$\overline{\varepsilon}_x = a_{11}\overline{\sigma}_x + a_{12}\overline{\sigma}_y + a_{16}\overline{\tau}_{xy}$$

$$\overline{\varepsilon}_y = a_{12}\overline{\sigma}_x + a_{22}\overline{\sigma}_y + a_{26}\overline{\tau}_{xy} \tag{A.3}$$

$$\overline{\gamma}_{xy} = a_{16}\overline{\sigma}_x + a_{26}\overline{\sigma}_y + a_{66}\overline{\tau}_{xy}$$

where a_{ij} are the compliances of the laminate.

Substituting Eq.(A.2) into Eq. (A.3) the following expression, which must be satisfied by the Airy stress function $F(x, y)$, is obtained.

$$a_{22}\frac{\partial^4 F}{\partial x^4} - 2a_{26}\frac{\partial^4 F}{\partial x^3 \partial y} + (2a_{12} + a_{66})\frac{\partial^4 F}{\partial x^2 \partial y^2} - 2a_{16}\frac{\partial^4 F}{\partial x \partial y^3} + a_{11}\frac{\partial^4 F}{\partial y^4} = 0 \tag{A.4}$$

Eq. (A.4) can be integrated using the following linear differential operators

$$D_1 D_2 D_3 D_4 F = 0 \tag{A.5}$$

where $D_k = \frac{\partial}{\partial y} - \mu_k \frac{\partial}{\partial x}$ $k = 1, ..., 4$

After the integration, Eq. (A.6) called as the characteristic equation is obtained.

$$a_{11}\mu^4 - 2a_{16}\mu^3 + (2a_{12} + a_{66})\mu^2 - 2a_{26}\mu + a_{22} = 0 \tag{A.6}$$

where μ_k are the roots of the characteristic equation.

For orthotropic plates $a_{16} = a_{26} = 0$ and the Eq. (A.6) reduces to:

$$\frac{\mu^4}{E_{xx}} + \left(\frac{1}{G_{xy}} - \frac{2\nu_{xy}}{E_{xx}} \right) \mu^2 + \frac{1}{E_{yy}} \tag{A.7}$$

Excluding special cases, μ_k are either complex or purely imaginary numbers. From Eq. (A.7), four roots in the form of μ_1, μ_2 and their conjugates $\overline{\mu}_1, \overline{\mu}_2$ are obtained. Among these roots two principal roots are chosen. According to a complementary definition, principal roots μ_1, μ_2 are always the complex roots that have the least value of argument among all roots. The principal roots depend on the relative sign of the quantities α_0 and β_0:

$$\alpha_0 = \sqrt{\frac{E_{xx}}{E_{yy}}} \quad , \quad \beta_0 = \left(\frac{E_{xx}}{2G_{xy}} - \nu_{xy} \right)$$

The roots are given below:

$$\mu_k = \frac{i}{\sqrt{2}} \left((-1)^{k+1} \sqrt{\beta_0 - \alpha_0} + \sqrt{\alpha_0 + \beta_0} \right) \quad , \quad \alpha_0 \leq \beta_0 \tag{A.8a}$$

$$\mu_k = \frac{i}{\sqrt{2}} \left((-1)^{k+1} \sqrt{\alpha_0 - \beta_0} + \sqrt{\alpha_0 + \beta_0} \right) \quad , \quad \alpha_0 > \beta_0 \tag{A.8b}$$

For isotropic plates, $\mu_1 = \mu_2 = i$. For laminates dominated by $\pm 45°$ plies, Berbinau et al. [38] state that the roots of the characteristic equation are of the form:

$$\mu_1 = F + iG \quad and \quad \mu_2 = -F + iG$$

Characteristic roots can be regarded as values, which define the degree of anisotropy in plane stress problems, and with these values one can judge how much a laminate can differ from the isotropic case.

Expression (A.5) can be rewritten as

$$D_4 F = g_3$$

$$D_3 D_4 F = g_2 \tag{A.9a}$$

$$D_2 D_3 D_4 F = g_1$$

$$D_1 g_1 \equiv \frac{\partial g_1}{\partial y} - \frac{\partial g_1}{\partial x} = 0 \tag{A.9b}$$

where $D_k, k = 1, ..., 4$ are partial derivatives of first order.

By integrating (A.9b), expression for g_1 is obtained.

$$g_1 = f_1(x + \mu_1 y) \tag{A.10}$$

In expression (A.10), f_1 is an arbitrary function of $x + \mu_1 y$. The integration of the set of equations in (A.9a) gives,

$$\frac{\partial g_2}{\partial y} - \mu_2 \frac{\partial g_2}{\partial x} = g_1$$

$$\frac{\partial g_3}{\partial y} - \overline{\mu}_1 \frac{\partial g_3}{\partial x} = g_2 \tag{A.11}$$

$$\frac{\partial F}{\partial y} - \overline{\mu}_2 \frac{\partial F}{\partial x} = g_3$$

By integrating non-homogeneous equations in (A.11) in order, the following expression for F is obtained.

$$F = F_1(x + \mu_1 y) + F_2(x + \mu_2 y) + F_3(x + \overline{\mu}_1 y) + F_4(x + \overline{\mu}_2 y) \tag{A.12}$$

Four different complex numbers for different variables are introduced.

$$z_1 = x + \mu_1 y$$

$$z_2 = x + \mu_2 y$$

$$z_3 = x + \overline{\mu}_1 y \tag{A.13}$$

$$z_4 = x + \overline{\mu}_2 y$$

Since stress function is a real function of x and y, for the case of different complex numbers presented in (A.12), the following relation can be written as

$$F = 2Re[F_1(z_1) + F_2(z_2)] \tag{A.14}$$

For the derivation of the stress components in terms of complex parameters, the following functions are defined

$$\phi_1(z_1) = \frac{dF_1}{dz_1}$$

$$\phi_2(z_2) = \frac{dF_2}{dz_2}$$

$$\phi_1'(z_1) = \frac{d\phi_1}{dz_1}$$ (A.15)

$$\phi_2'(z_1) = \frac{d\phi_2}{dz_2}$$

Stress components in Eq. (A.1) can be written in terms of the functions defined in Eq. set (A.15)

$$\sigma_x = 2Re[\mu_1^2\phi_1'(z_1) + \mu_2^2\phi_2'(z_2)]$$

$$\sigma_y = 2Re[\phi_1'(z_1) + \phi_2'(z_2)]$$ (A.16)

$$\tau_{xy} = -2Re[\mu_1\phi_1'(z_1) + \mu_2\phi_2'(z_2)]$$

The problem of a plate containing a hole can be solved by using the principle of superposition [39].
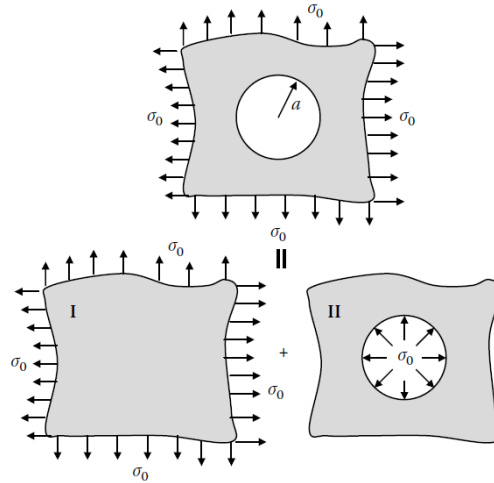
Figure A.1: Total stress in an infinite plate with a circular opening can be decomposed into two stress states I and II.

As shown in Figure A.1, infinite plate with a circular opening problem can be solved by super-positioning stress state I, which resembles the uniform stress distribution,

66

plus stress state II, which is caused by the circular opening in the infinite plate. Tan's definition for the orthotropic plate with an elliptical opening subjected to combined loading represented in Figure A.2 [16].
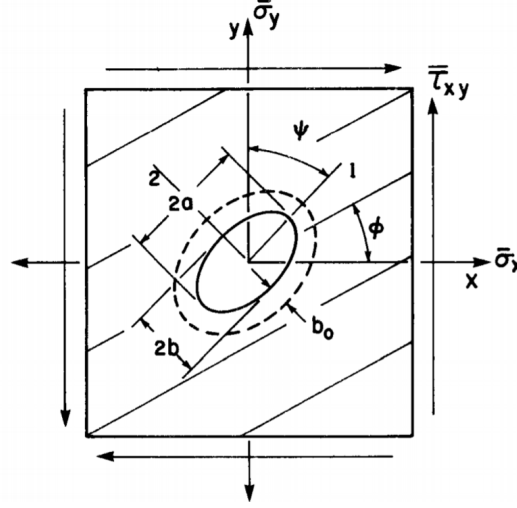
Figure A.2: Coordinates of a composite lamina with an elliptical opening subjected to combined loading [16].

Uniform stress field can be expressed as:

$$(\sigma'_1)^0 = \overline{\sigma}_x \sin^2 \psi + \overline{\sigma}_y \cos^2 \psi + \overline{\tau}_{xy} \sin 2\psi$$
$$(\sigma'_2)^0 = \overline{\sigma}_x \cos^2 \psi + \overline{\sigma}_y \sin^2 \psi + \overline{\tau}_{xy} \sin 2\psi \qquad \text{(A.17)}$$
$$(\sigma'_6)^0 = (\overline{\sigma}_y - \overline{\sigma}_x) \sin \psi \cos \psi - \overline{\tau}_{xy} \cos 2\psi$$

Stress components due to opening:

$$\sigma_x = 2Re\left[\mu_1^2 \phi'_1(z_1) + \mu_2^2 \phi'_2(z_2)\right]$$
$$\sigma_y = 2Re\left[\phi'_1(z_1) + \phi'_2(z_2)\right] \qquad \text{(A.18)}$$
$$\tau_{xy} = -2Re\left[\mu_1 \phi'_1(z_1) + \mu_2 \phi'_2(z_2)\right]$$

The total in-plane laminate stress components given in the principal coordinates of the opening are composed of the stresses caused by the uniform stress field, Eq. (A.17),

67

plus the stresses due to opening, Eq. (A.18).

$$\sigma_1 = (\sigma_1')^0 + 2Re\left[\mu_1^2\phi_1'(z_1) + \mu_2^2\phi_2'(z_2)\right]$$

$$\sigma_2 = (\sigma_2')^0 + 2Re\left[\phi_1'(z_1) + \phi_2'(z_2)\right]$$

$$\sigma_6 = (\sigma_6')^0 + -2Re\left[\mu_1\phi_1'(z_1) + \mu_2\phi_2'(z_2)\right]$$

Substituting the values of $\phi_1(z_1)$ and $\phi_2(z_2)$, stress functions for the laminate with an open hole can be written as [38],

$$\sigma_1 = (\sigma_1')^0 + Re\left[\frac{i}{\mu_1 - \mu_2}\left[\mu_1^2 h_1(z_1, \mu_1) + \mu_2^2 h_2(z_2, \mu_2)\right]\right]$$

$$\sigma_2 = (\sigma_2')^0 + Re\left[\frac{i}{\mu_1 - \mu_2}\left[h_1(z_1, \mu_1) + h_2(z_2, \mu_2)\right]\right]$$

$$\sigma_6 = (\sigma_6')^0 - Re\left[\frac{i}{\mu_1 - \mu_2}\left[\mu_1 h_1(z_1, \mu_1) + \mu_2 h_2(z_2, \mu_2)\right]\right]$$

where

$$h_k(z_k, \mu_k) = \frac{(-1)^{k+1}b^2(c - i\mu_k)\left[p(1 + ic\lambda\mu_{3-k}) + t(ic + \mu_{3-k})\right]}{\sqrt{z_k^2 - b^2(c^2 + \mu_k^2)}\left(z_1 + \sqrt{z_k^2 - b^2(c^2 + \mu_k^2)}\right)} \quad , \quad k = 1, 2$$

Up to this point, stress field solutions are written for infinite anisotropic plates. To apply these results to a finite width plate, a correction factor is needed to account for the finite width effect. In Figure A.3, a finite width anisotropic laminate with an elliptical opening is displayed.

The relation to account for finite width correction is expressed as

$$\begin{Bmatrix} \overline{\sigma}_x \\ \overline{\sigma}_y \\ \overline{\sigma}_{xy} \end{Bmatrix} = f_{correction}\left(\frac{W}{2a}\right) \begin{Bmatrix} \overline{\sigma}_x \\ \overline{\sigma}_y \\ \overline{\sigma}_{xy} \end{Bmatrix}_{W=\infty} \tag{A.19}$$

where

$$\frac{W}{2a} : \frac{plate\ width}{major\ diameter}$$

$f_{correction}$ is the approximate orthotropic finite width correction for a circular hole opening ($a = b$) as a function of $W/2a$. The correction factor is expressed explicitly as [12]

$$f_{correction} = \frac{K_T^\infty}{K_T} = \frac{3(1 - D/W)}{2 + (1 - D/W)^3} + \frac{1}{2}\left(\frac{D}{W}M\right)^6 (K_T^\infty - 3)\left[1 - \left(\frac{D}{W}M\right)^2\right]$$

$$\tag{A.20}$$

68
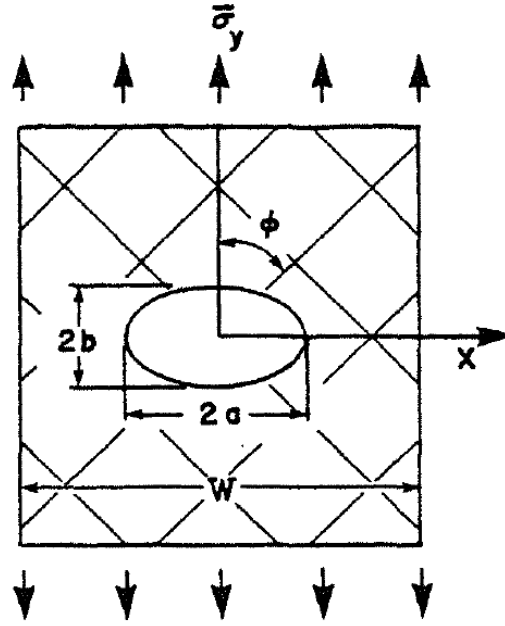
Figure A.3: A finite width anisotropic plate with an elliptical opening.

where

$$M = \sqrt{\frac{\sqrt{1 - 8\left[\frac{3(1-D/W)}{2+(1-D/W)^3} - 1\right]} - 1}{2\left(D/W\right)^2}} \quad , \quad D = 2a$$

K_T and K_T^∞ are stress concentration factors for finite and infinite plates, respectively. M is defined as the magnification factor and implemented to get more accurate results for $a/b < 4$. For quasi-isotropic plates, a simpler relation is introduced

$$f_{correction} = \frac{K_T^\infty}{K_T} = \frac{3\left(1 - D/W\right)}{2 + \left(1 - D/W\right)^3} \tag{A.21}$$

In both Eqs. (A.20) and (A.21), the ratio of the major diameter to the plate width $(2a/W)$ is selected as

- in the case of a circular hole $(a = b)$

$$\frac{W}{2a} = \min\left(\frac{W_x}{2a}, \frac{W_y}{2a}\right)$$

- in the case of an elliptical hole

$$\frac{W}{2a} = \min\left(\frac{W_x}{2a}, \frac{W_y}{2b}\right)$$

APPENDIX B

CLASSICAL LAMINATION THEORY(CLT)

In this chapter, obtaining of the layer stresses using CLT is explained. The steps for calculating the layer stresses as follows

Required inputs are

- Ply thickness, ply sequence and material orientation angle

- Mechanical loading (Forces $[N]_{x,y}$ and Moments $[M]_{x,y}$)

- Elastic properties (E_1, E_2, ν_{12}, G_{12})

Poisson's ratio ν_{12} is calculated

$$\nu_{12} = E_2 \frac{\nu_{12}}{E_1}$$
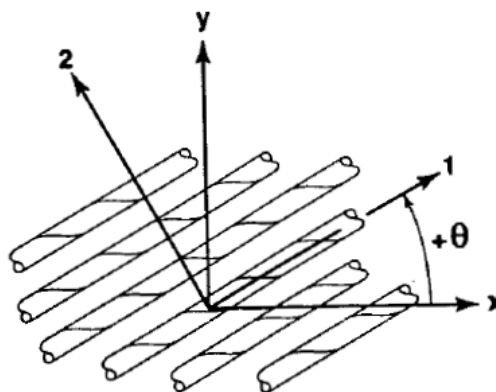
Figure B.1: Rotation of Principal Material Axes from x-y Axes.

Reduced ply stiffnesses $[Q]_{1,2}$ with respect to material principal axis are computed

$$Q_{11} = \frac{E_1}{1 - \nu_{12}\nu_{21}}$$
$$Q_{22} = \frac{E_2}{1 - \nu_{12}\nu_{21}}$$
$$Q_{12} = \frac{\nu_{21}E_1}{1 - \nu_{12}\nu_{21}}$$
$$Q_{66} = G_{12}$$

Transformed reduced stiffnesses with respect to laminate reference axes (x, y) are calculated for each layer (k)

$$Q_{xx} = Q_{11}m^4 + 2(Q_{12} + 2Q_{66})n^2m^2 + Q_{22}n^4$$
$$Q_{yy} = Q_{11}n^4 + 2(Q_{12} + 2Q_{66})n^2m^2 + Q_{22}m^4$$
$$Q_{xy} = (Q_{11} + Q_{22} - 4Q_{66})n^2m^2 + Q_{12}(n^4 + m^4)$$
$$Q_{xs} = (Q_{11} - Q_{12} - 2Q_{66})nm^3 + (Q_{12} - Q_{22} + 2Q_{66})n^3m$$
$$Q_{ys} = (Q_{11} - Q_{12} - 2Q_{66})n^3m + (Q_{12} - Q_{22} + 2Q_{66})nm^3$$
$$Q_{ss} = (Q_{11} + Q_{22} - 2Q_{12} - 2Q_{66})n^2m^2 + Q_{66}(n^4 + m^4)$$

where $n = sin(\theta), \quad m = cos(\theta)$

Through the thickness coordinate, z_k, for each layer (k) is calculated
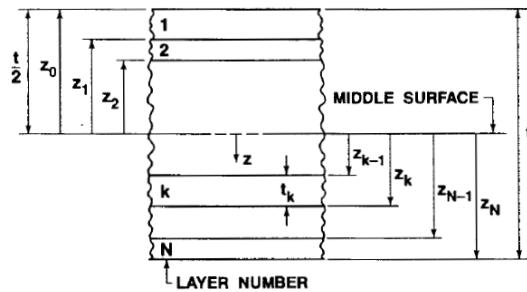
Figure B.2: Geometry of an N-Layered Laminate.

Laminate stiffness matrices $[A], [B]$ and $[D]$ are computed.

$$A_{ij} = \sum_{k=1}^{n} Q_{ij}(z_k - z_{k-1})$$

$$B_{ij} = \frac{1}{2}\sum_{k=1}^{n} Q_{ij}(z_k^2 - z_{k-1}^2)$$

$$D_{ij} = \frac{1}{3}\sum_{k=1}^{n} Q_{ij}(z_k^3 - z_{k-1}^3)$$

Laminate compliance matrices are computed

$$[a] = [A^{-1}] - [B^*][D^{*-1}][C^*]$$

$$[b] = [B^*][D^{*-1}]$$

$$[c] = -[D^{*-1}][C^*]$$

$$[d] = [D^{*-1}]$$

where

$$[A^{-1}] = \textit{inverse of matrix } [A]$$

$$[B^*] = -[A^{-1}][B]$$

$$[C^*] = [B][A^{-1}]$$

$$[D^*] = [D] - [B][A^{-1}][B]$$

Reference plane strains $[\varepsilon^o]_{x,y}$ and curvatures $[\kappa]_{x,y}$ are calculated

$$
\begin{bmatrix} \varepsilon_x^o \\ \varepsilon_y^o \\ \gamma_s^o \\ \kappa_x \\ \kappa_y \\ \kappa_s \end{bmatrix}
=
\begin{bmatrix}
a_{xx} & a_{xy} & a_{xs} & b_{xx} & b_{xy} & b_{xs} \\
a_{yx} & a_{yy} & a_{ys} & b_{yx} & b_{yy} & b_{ys} \\
a_{sx} & a_{sy} & a_{ss} & b_{sx} & b_{sy} & b_{ss} \\
c_{xx} & c_{xy} & c_{xs} & d_{xx} & d_{xy} & d_{xs} \\
c_{yx} & c_{yy} & c_{ys} & d_{yx} & d_{yy} & d_{ys} \\
c_{sx} & c_{sy} & c_{ss} & d_{sx} & d_{sy} & d_{ss}
\end{bmatrix}
\begin{bmatrix} N_x \\ N_y \\ N_s \\ M_x \\ M_y \\ M_s \end{bmatrix}
$$

Through the thickness coordinate of the lamina mid-plane $(\overline{z}_k)$ is calculated

$$\overline{z}_k = \frac{z_k + z_{k+1}}{2}$$

Strains at each layer in the laminate with reference to laminate coordinates system is

73

determined

$$
\begin{bmatrix} \varepsilon_x \\ \varepsilon_y \\ \varepsilon_s \end{bmatrix} = \begin{bmatrix} \varepsilon_x^o \\ \varepsilon_y^o \\ \gamma_s^o \end{bmatrix} + z \begin{bmatrix} \kappa_x \\ \kappa_y \\ \kappa_s \end{bmatrix}
$$

Layer strains $[\varepsilon]_{1,2}^k$ with respect to material principal axis $(1, 2)$ using the transformation matrix is calculated

$$
\begin{bmatrix} \varepsilon_1 \\ \varepsilon_2 \\ \frac{1}{2}\gamma_6 \end{bmatrix} = \begin{bmatrix} m^2 & n^2 & 2mn \\ n^2 & m^2 & -2mn \\ -mn & mn & m^2 - n^2 \end{bmatrix} + z \begin{bmatrix} \varepsilon_x \\ \varepsilon_y \\ \varepsilon_s \end{bmatrix}
$$

where $n = sin(\theta), \quad m = cos(\theta)$

Layer stresses $[\sigma]_{1,2}^k$ with respect to material principal axis $(1, 2)$ are calculated

$$
\begin{bmatrix} \sigma_1 \\ \sigma_2 \\ \tau_6 \end{bmatrix} = \begin{bmatrix} Q_{11} & Q_{12} & 0 \\ Q_{12} & Q_{22} & 0 \\ 0 & 0 & Q_{66} \end{bmatrix} + z \begin{bmatrix} \varepsilon_1 \\ \varepsilon_2 \\ \gamma_6 \end{bmatrix}
$$

APPENDIX C

EXPERIMENTAL RESULTS

In-situ and post mortem images and load displacement curves of tested specimens are given in this chapter.

OHT1-1-1
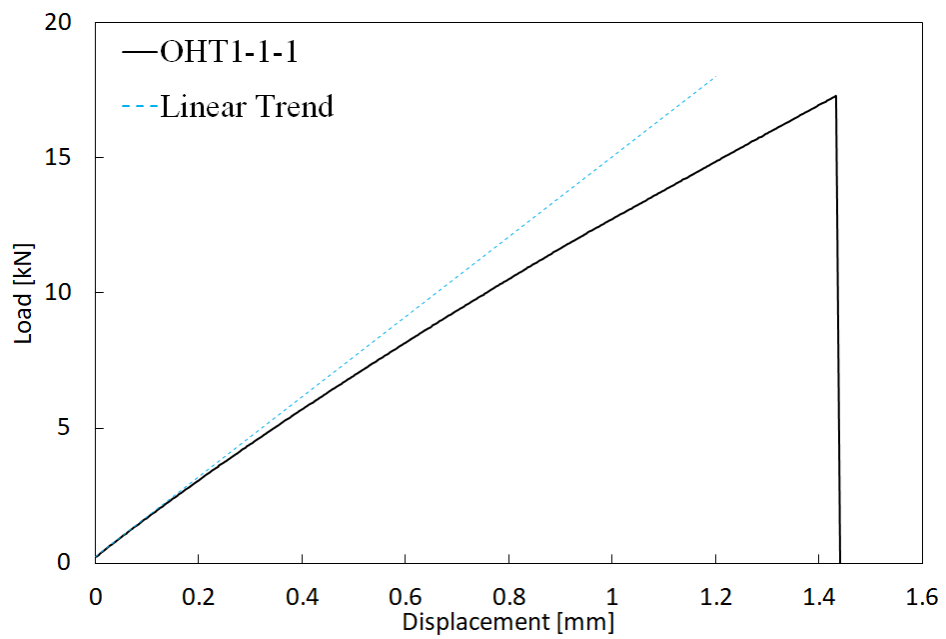
Figure C.1: Load displacement curve of the OHT1-1-1 test specimen.
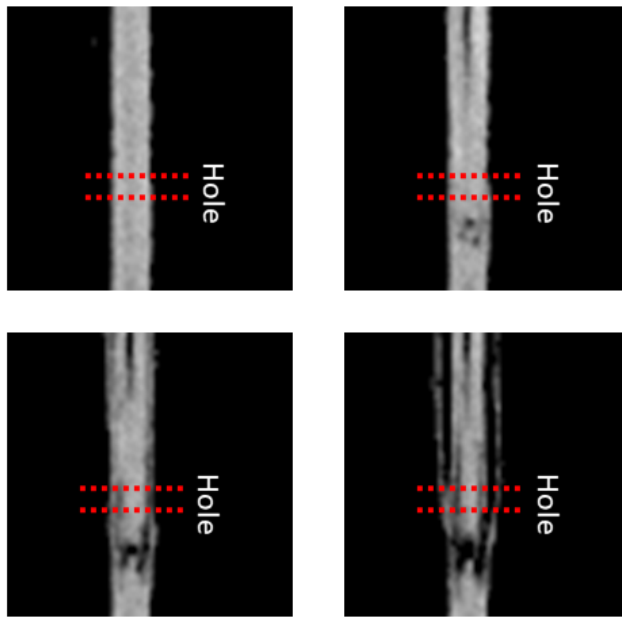
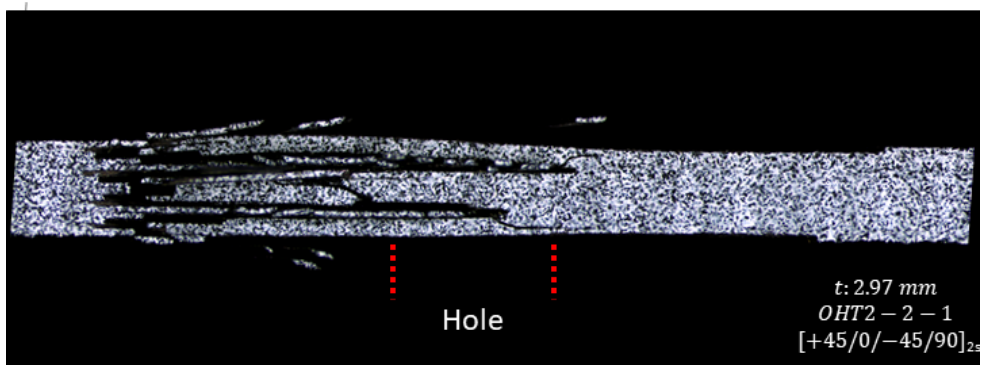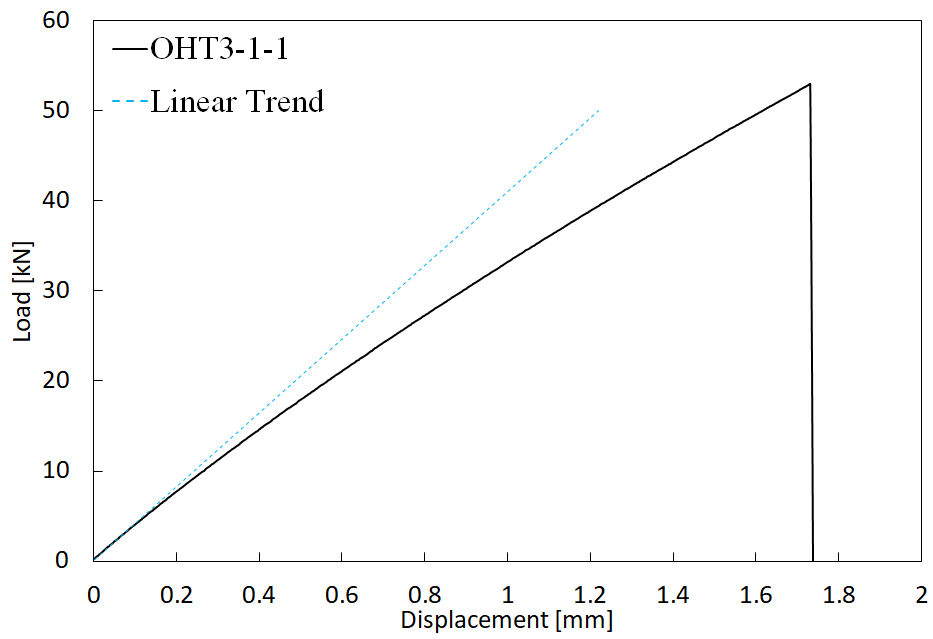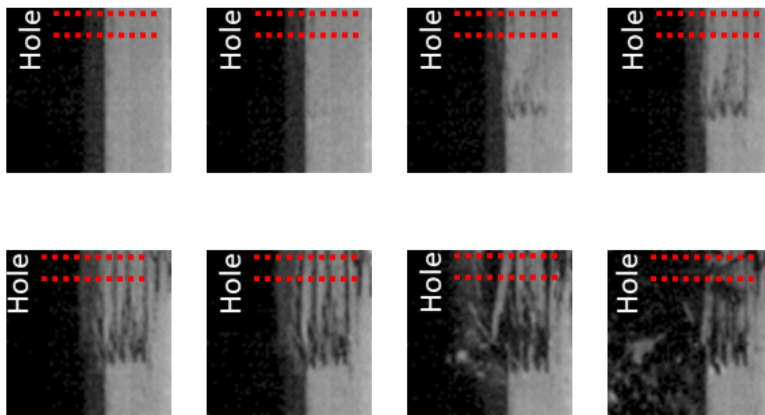Figure C.2: High speed camera images of the OHT1-1-1 test specimen at 581250 fps.
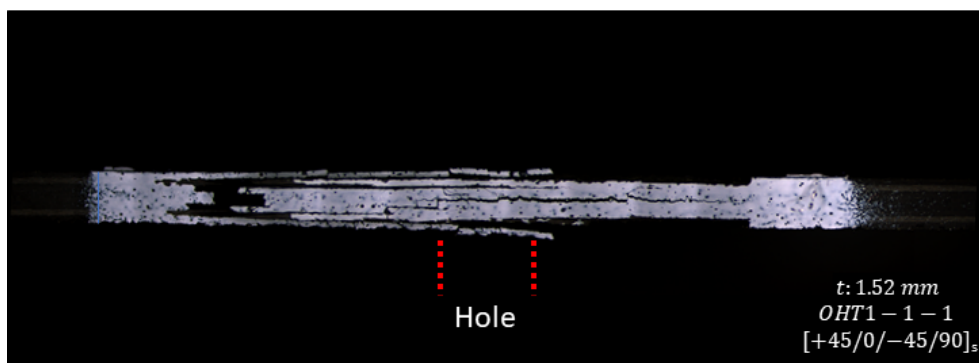
Figure C.3: Post mortem image of the OHT1-1-1 test specimen at 50x magnification.

OHT2-1-1
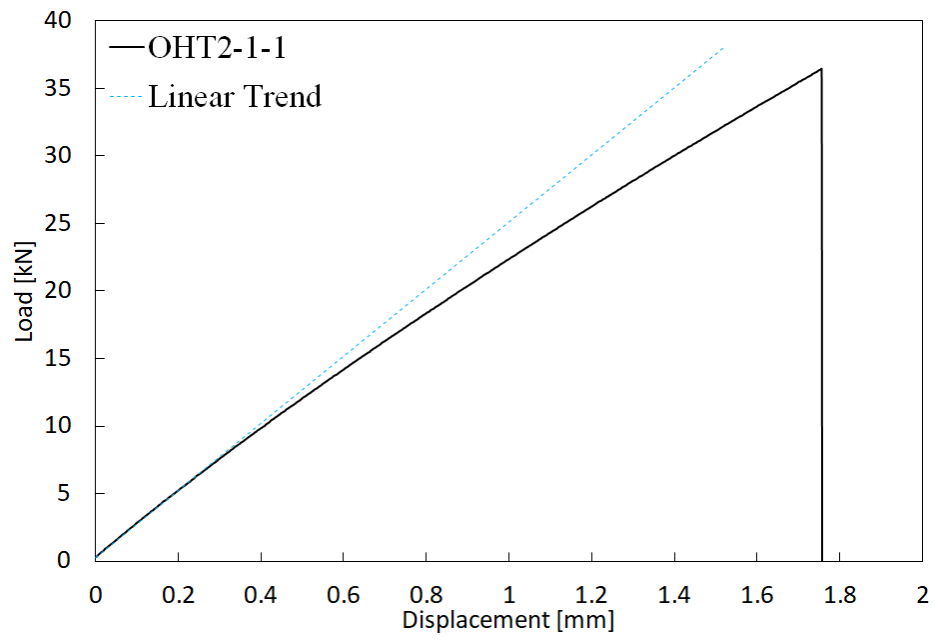
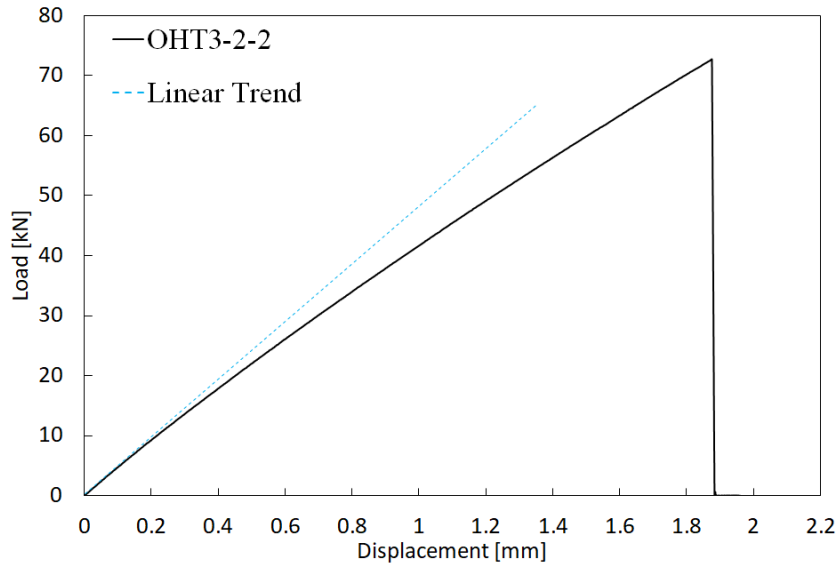Figure C.4: Load displacement curve of the OHT2-1-1 test specimen.
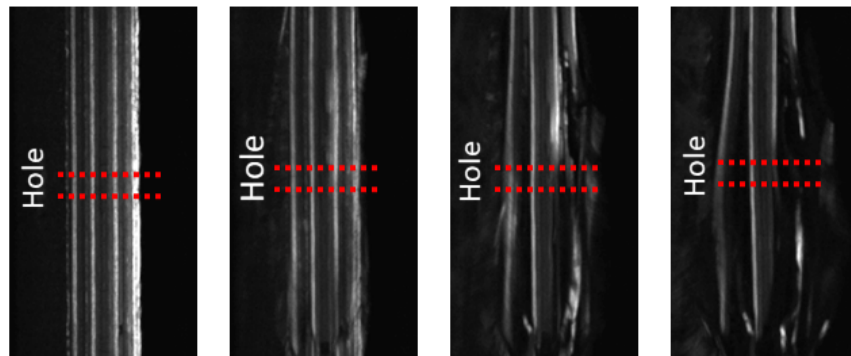
Figure C.5: High speed camera images of the OHT2-1-1 test specimen at 150000 fps.
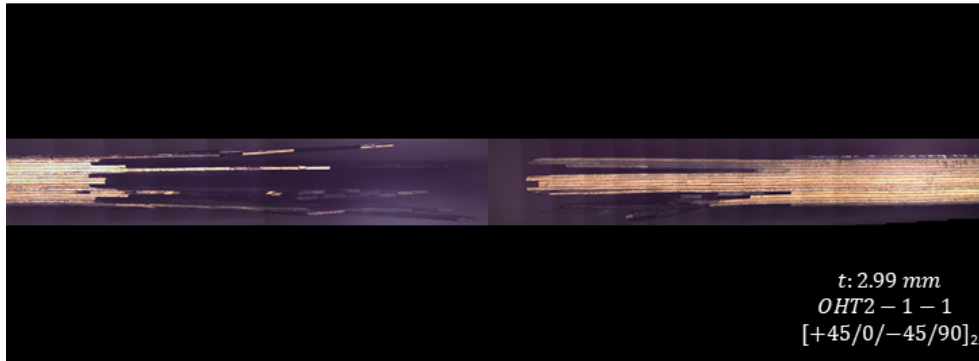
Figure C.6: Post mortem image of the OHT2-1-1 test specimen at 50x magnification.

OHT2-2-1
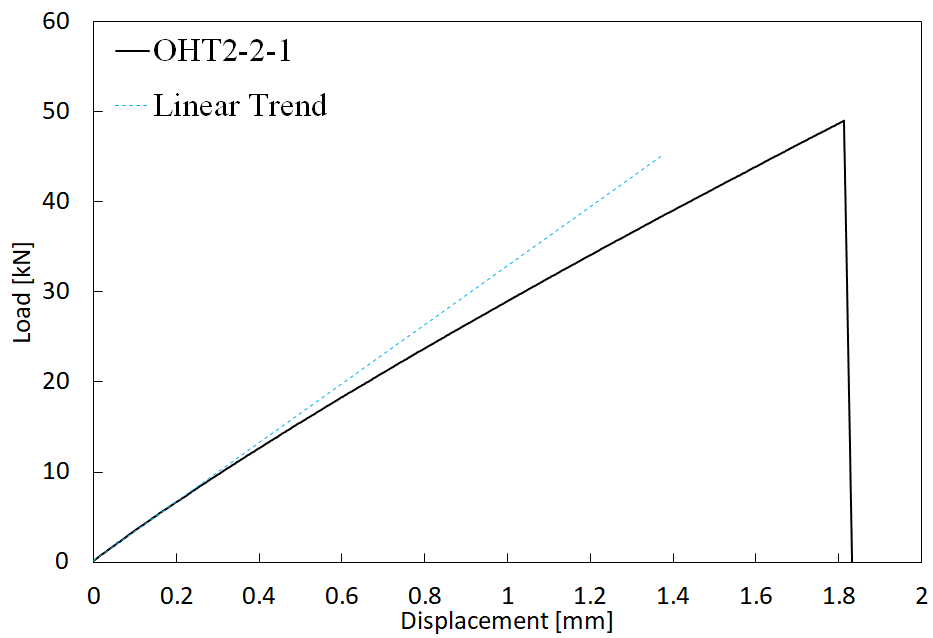
Figure C.7: Load displacement curve of the OHT2-2-1 test specimen.
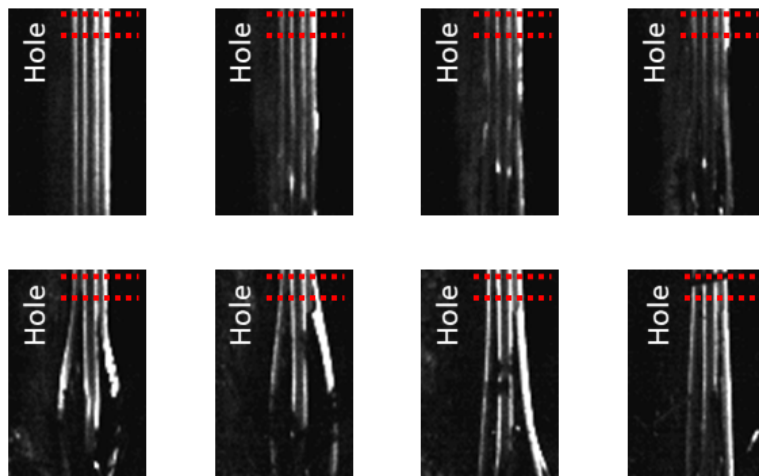
Figure C.8: High speed camera images of the OHT2-2-1 test specimen at 420000 fps.

Figure C.9: Post mortem image of the OHT2-2-1 test specimen at 50x magnification.

OHT3-1-1

Figure C.10: Load displacement curve of the OHT3-1-1 test specimen.

Figure C.11: High speed camera images of the OHT3-1-1 test specimen at 581250 fps.
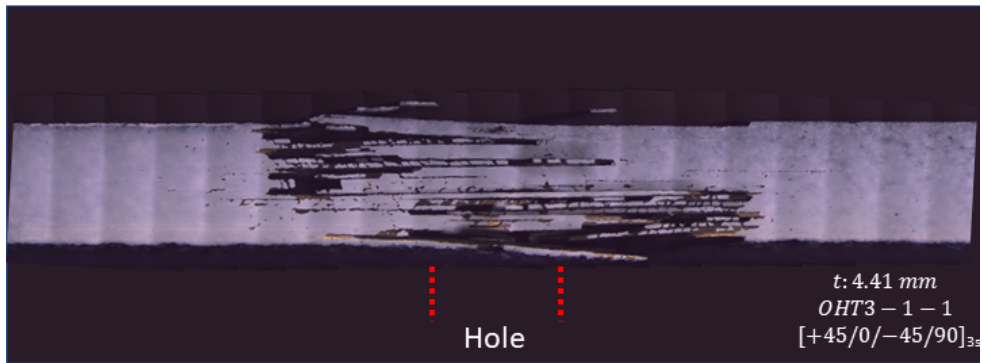
Figure C.12: Post mortem image of the OHT3-1-1 test specimen at 50x magnification.

OHT3-2-1
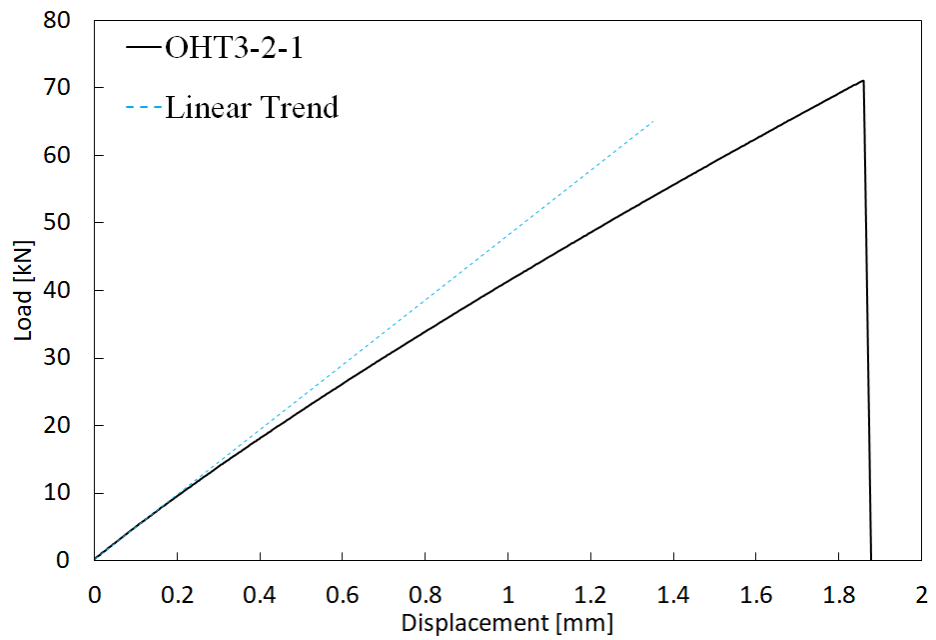
Figure C.13: Load displacement curve of the OHT3-2-1 test specimen.

OHT3-2-2

Figure C.14: Load displacement curve of the OHT3-2-2 test specimen.

OHT3-2-3
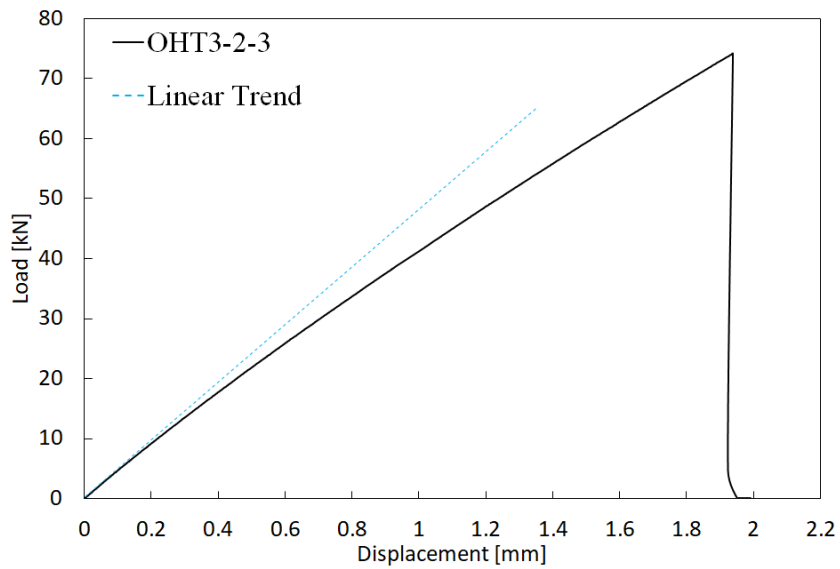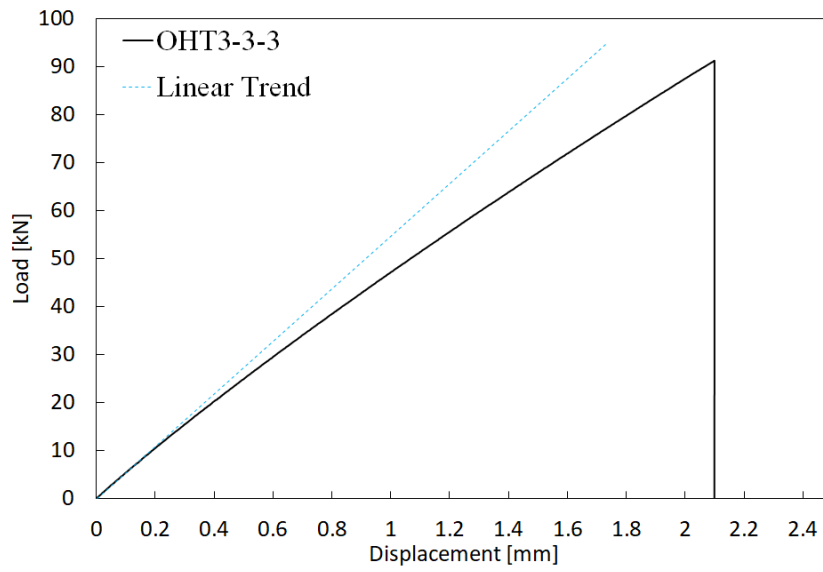

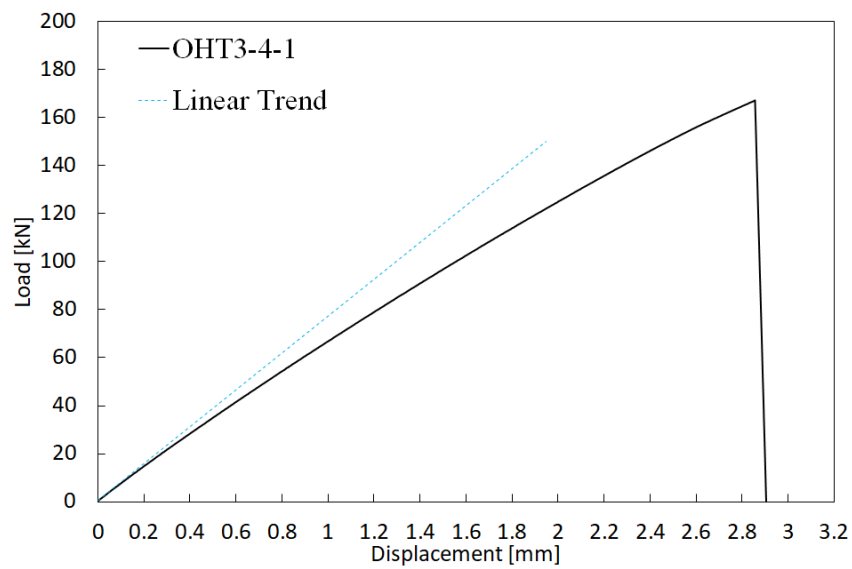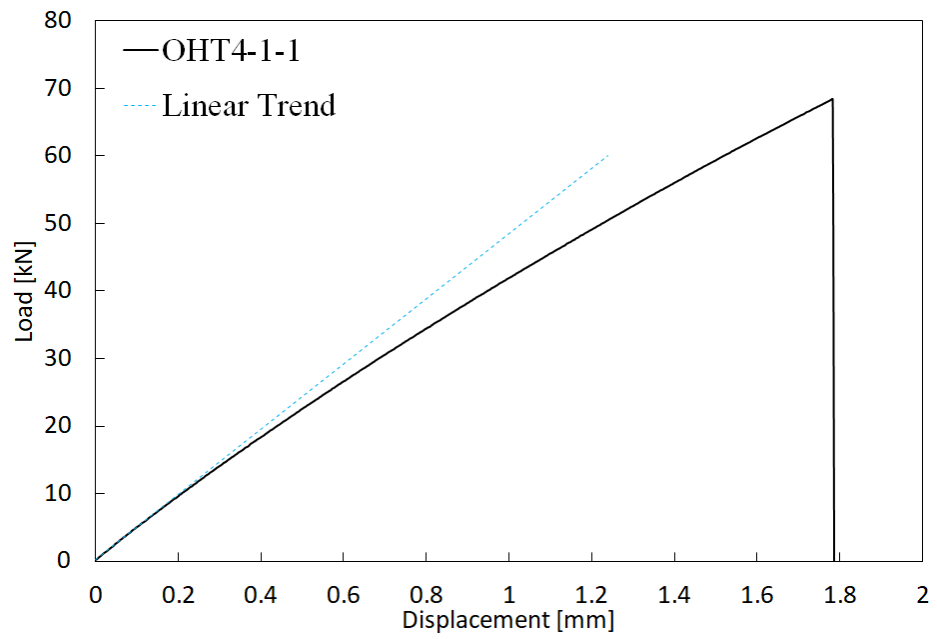Figure C.15: Load displacement curve of the OHT3-2-3 test specimen.

OHT3-3-1
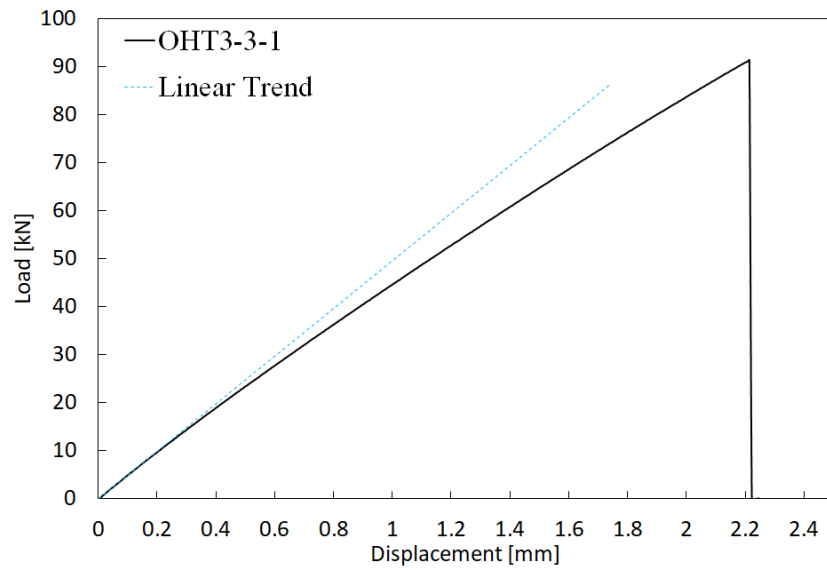
Figure C.16: Load displacement curve of the OHT3-3-1 test specimen.

OHT3-3-2
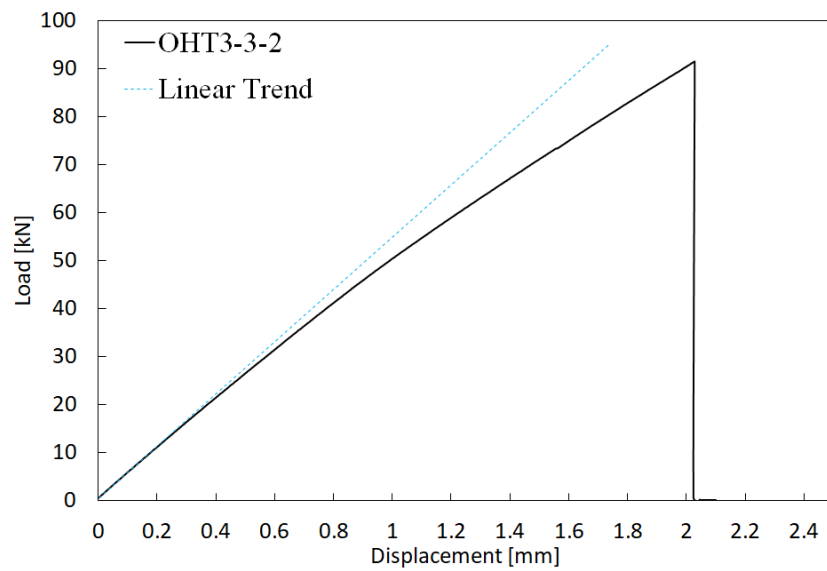
Figure C.17: Load displacement curve of the OHT3-3-2 test specimen.

OHT3-3-3

Figure C.18: Load displacement curve of the OHT3-3-3 test specimen.

OHT3-4-1

Figure C.19: Load displacement curve of the OHT3-4-1 test specimen.

OHT4-1-1

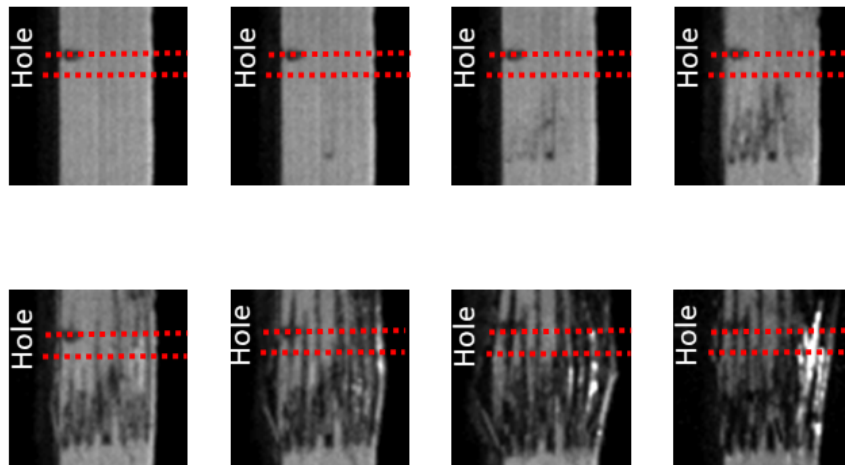Figure C.20: Load displacement curve of the OHT4-1-1 test specimen.

Figure C.21: High speed camera images of the OHT4-1-1 test specimen at 581250 fps.
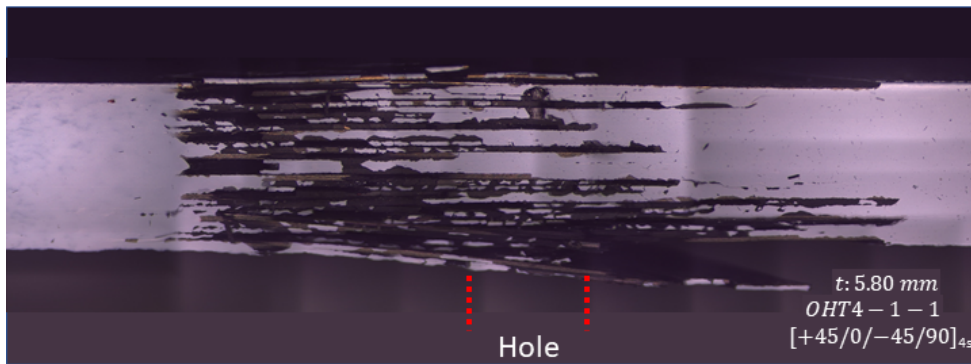
Figure C.22: Post mortem image of the OHT4-1-1 test specimen at 50x magnification.